Title

Deciphering Distinct Overpotential-Dependent Pathways for Electrochemical CO2 Reduction Catalyzed by an Iron—Terpyridine Complex

Journal

Inorganic Chemistry, 61(18)

ISSN

0020-1669

Authors

Loipersberger, Matthias
Derrick, Jeffrey S
Chang, Christopher J
et al.

Publication Date

2022-05-09

DOI

10.1021/acs.inorgchem.2c00279

Deciphering Distinct Overpotential Dependent Pathways for Electrochemical CO_2 Reduction Catalyzed by an Iron-Terpyridine Complex.

Matthias Loipersberger[1‡], Jeffrey S. Derrick[1,2‡], Christopher J. Chang[1,2,3*], Martin Head-Gordon[1,2*]

[1]Department of Chemistry University of California, Berkeley, CA, 94720

[2]Chemical Sciences Division, Lawrence Berkeley National Laboratory, Berkeley, CA, 94720, USA

[3]Department of Molecular and Cell Biology University of California, Berkeley, CA, 94720, USA

‡Contributed equally

ABSTRACT: $[Fe(tpyPY2Me)]^{2+}$ ($[Fe]^{2+}$) is a homogeneous electrocatalyst for converting CO_2 into CO featuring low overpotentials of <100 mV, near-unity selectivity, and high activity with turnover frequencies faster than 100,000 s^{-1}. To identify the origins of its exceptional performance and inform future catalyst design, we report a combined computational and experimental study that establishes two distinct mechanistic pathways for electrochemical CO_2 reduction catalyzed by $[Fe]^{2+}$ as a function of applied overpotential. Electrochemical data shows the formation of two catalytic regimes at low ($\eta_{TOF/2}$ of 160 mV) and high ($\eta_{TOF/2}$ of 590 mV) overpotential plateaus. We propose that at low overpotentials $[Fe]^{2+}$ undergoes a two-electron reduction, two-proton transfer mechanism (electrochemical-electrochemical-chemical-chemical, EECC), where turnover occurs through the dicationic iron complex, $[Fe]^{2+}$. Computational analysis supports the importance of the singlet ground state electronic structure for CO_2 binding and that the rate-limiting step is the second protonation in this low-overpotential regime. When more negative potentials are applied, an additional electron transfer event occurs through either a stepwise or proton-coupled electron transfer (PCET) pathway, enabling catalytic turnover from the monocationic iron complex ($[Fe]^{+}$) via an electrochemical-chemical-electrochemical-chemical (ECEC) mechanism. Comparison of experimental kinetic data obtained from variable controlled potential electrolysis (CPE) experiments with direct product detection with calculated rates obtained from the energetic span model support the PCET pathway as the most likely mechanism. Moreover, we build upon this mechanistic understanding to propose the design of an improved ligand framework that is predicted to stabilize the key transition states identified from our study and explore their electronic structures using an energy decomposition analysis. Taken together, this work highlights the value of synergistic computational/experimental approaches to decipher mechanisms of new electrocatalysts and direct the rational design of improved platforms

INTRODUCTION

Increasing energy demands and global climate change motivate the need for technologies that capture and utilize atmospheric carbon dioxide (CO_2) and convert it into value-added carbon products.[1–3] In this context, the electrochemical reduction of CO_2[4,5] offers a promising way to restore balance to the carbon cycle and develop a net negative carbon footprint if these technologies can be coupled to renewable sources of electricity. A diverse array of upgraded carbon products for the electrochemical CO_2 reduction reaction (CO_2RR) include CO, CH_3OH, and CH_4.[6] Of these products, the two-electron two-proton reduction of CO_2 to CO is economically most viable due to its usage in the Fischer-Tropsch process.[7]

In order to realize the goal of sustainable electrochemical carbon capture and conversion, efficient catalysts are required to selectively drive CO_2 reduction versus the thermodynamic and kinetically competitive hydrogen evolution reaction (HER).[5,8] The electrochemical CO_2 reduction reaction has been extensively explored across materials,[9] biological,[10] and molecular systems.[11] Molecular electrocatalysts are of particular interest as they are ideal platforms that can be rationally and systematically tuned through synthetic chemistry[12–14] with a level of precision and in the absence of defects that is unavailable to heterogeneous congeners.[9,15] Moreover, owing to their small size relative to enzymes and their homogeneous nature, they can be investigated at a mechanistic level which aids in the understanding and directed development of improved catalytic platforms.[14,16,17]

In this regard, iron-based molecular systems are especially desirable owing to the abundance of this element; the iron porphyrin platform Fe-TPP (TPP = tetraphenylporphyrin) is a robust and active catalyst making it a popular framework for ligand development with a considerable number of derivatives having been prepared in recent years.[18–28] The turnover frequency of the original Fe-TPP platform has been improved by several orders of magnitude from 10^2 s^{-1} to 10^6 s^{-1} for Fe-*o*-TMA, a tetra-substituted trimethylanilinium, derivative. The (current) top performance of 10^9 s^{-1} for Fe-TPP-based catalysts is achieved by introducing four bulky, methylimidazolium-containing groups.[29] The success story of the Fe-TPP system illustrates the effectiveness of systematic synthetic modification of the ligand scaffold and optimization of reaction conditions. Alternatively, simpler polypyridyl ligand platforms, including iron-bipyridine (bpy)[30,31] (Figure 1a) and iron-quaterpyridine (qpy)[32–35] (Figure 1c), have received increased attention for

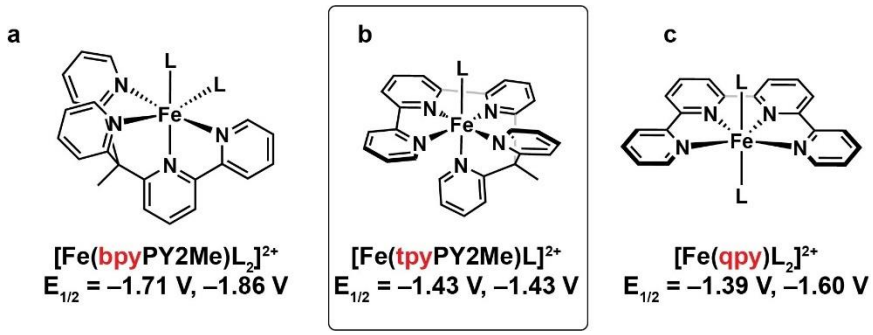

Figure 1. Overview of select iron polypyridyl molecular catalyst platforms for CO_2 reduction. Chemical structures of (a) $[Fe(bpyPY2Me)L_2]^{2+}$, (b) $[Fe(tpyPY2Me)L]^{2+}$, and (c) $[Fe(qpy)L_2]^{2+}$. Redox potentials for the iron catalyst are provided versus Fc/Fc^+. $[Fe(tpyPY2Me)L]^{2+}$ exhibits two single electron reduction events that are poorly resolved and centered at –1.43 V vs Fc/Fc^+. L = H_2O or CH_3CN.

electrochemical CO_2 reduction chemistry. These systems are robust under electrochemical conditions and are synthetically accessible through facile and modular routes which facilitates precise tuning of their sterics and electronics in a rational fashion.

Against this backdrop, the development of novel metal-polypyridyl electrocatalysts for proton and CO_2 reduction has been a part of a larger research program between our laboratories in energy conversion chemistry.[30,31,36–38] We recently reported[39] a novel terpyridine (tpy)-based iron polypyridine complex (Figure 1b), $[Fe(tpyPY2Me)]^{2+}$ ($[Fe]^{2+}$), that leverages ligand non-innocence of the tpy moiety and metal-ligand cooperativity through exchange coupling. These two factors yield mild reduction potentials for the complex in comparison to other pyridine-based catalysts as illustrated in Figure 1 and enables it to electrochemically convert CO_2 into CO at extremely low overpotentials (η), resulting in high product selectivity and rates under both organic solvents and aqueous conditions. The Faradaic efficiency for CO production (FE_{CO}), rates (k_{max}) and overpotentials of the three platforms are compared to the Fe-TPP platforms and summarized in Table 1. Comparison of these parameters clearly identifies these polypyridyl complexes as some of the best homogeneous catalysts to date, but we note that benchmarking should be done with care and caution. Indeed, determination of accurate overpotentials requires the use of the thermodynamic potential required to convert CO_2 into CO, which is often unknown for the exact experimental conditions and can thus vary by over 500 mV depending on solution conditions. To normalize for this uncertainly, we give the values reported by Matsubara[40] that take into account the effect of solvent mixtures, acid additives, and homoconjugation of phenol in acetonitrile.[40–43] Similarly, estimation of kinetic performance based on the maximum turnover frequency (TOF_{max}) is highly dependent on the method utilized (*e.g.*, foot-of-the-wave analysis, peak catalytic current analysis, etc).[44–48] As such, the methods used to determine the rates are indicated in Table 1. Specifically, in order to minimize uncertainty in rate determination for our $[Fe]^{2+}$ catalyst, we extracted the kinetic parameters directly from the averaged specific current densities for CO production obtained from variable potential CPE experiments that were conducted in triplicate as described by Savéant and coworkers.[49,50]

In our initial study of the $[Fe(tpyPY2Me)]^{2+}$ system, we reported the synthesis, characterization, and electrocatalytic behavior of $[Fe]^{2+}$ for CO_2RR to CO. Synthesis of the two-electron reduced product, $[Fe(tpyPY2Me)]^0$ ($[Fe]^0$), and spectroscopic characterization enabled us to attribute its exceptional catalytic activity to its unique open-shell singlet electronic structure that results from the antiferromagnetic coupling of the intermediate-spin Fe(II) center (S_{Fe} = 1) to a doubly reduced, triplet ligand system (S_{tpy} = 1). We were able to establish that this electronic structure was responsible for the reduction of CO_2 to CO at low overpotentials, through the preparation and comparison to a series of redox-(in)active metal and ligand controls. However, despite a detailed understanding of the electronic structure of

Table 1. Key benchmark metrics for the three pyridine based catalytic platforms and direct comparison to the TPP frameworks. Rates for $[Fe(bpy^{NHEt}PY2Me)L_2]^{2+}$ and FeTPP were determined by FOWA. Rates for $[Fe(qpy)(H_2O)_2]^{2+}$ and Fe-*o*-TMA were measured with catalytic plateau analysis and from bulk electrolysis current. $[Fe(tpyPY2Me)]^{2+}$ rates were extracted directly from the averaged specific current densities for CO production obtained from variable potential CPE experiments that were conducted in triplicate.

Platform	FE_{CO} (%)	TOF_{max} (s^{-1})	h_{eff} (V)	Ref.
$[Fe(bpy^{NHEt}PY2Me)L_2]^{2+}$	81	10^2	0.66	[30]
$[Fe(tpyPY2Me)]^{2+}$	97	10^5	0.71	[39]
$[Fe(qpy)(H_2O)_2]^{2+}$	70	10^2	0.24	[33]
FeTPP	93	10^2	0.67	[40]
Fe-*o*-TMA	93	10^6	0.60	[22,40]

the $[Fe]^{2+}$ system and its two-electron reduced product, the mechanism(s) through which it functions in CO_2RR are insufficiently explored. In the present study, we use a combined experimental and computational approach to identify two distinct mechanistic pathways for CO_2RR catalyzed by $[Fe(tpyPY2Me)]^{2+}$ depending on applied overpotential, η. We propose that at low overpotentials [$E_{cat/2}$ of –1.43 V vs Fc/Fc^+ ($\eta_{TOF/2}$ = 0.16 V)], $[Fe]^{2+}$ undergoes a two-electron reduction, two-proton transfer mechanism (electrochemical-electrochemical-chemical-chemical, EECC) where turnover occurs though the dicationic iron complex, $[Fe]^{2+}$. At higher overpotentials [$E_{cat/2}$ of –1.86 V vs Fc/Fc^+ ($\eta_{TOF/2}$ = 0.59 V)], an additional electron transfer event becomes possible through either a stepwise or a proton-coupled electron transfer (PCET) pathway, enabling catalytic turnover from the monocationic iron complex ($[Fe]^+$) via an electrochemical-chemical-electrochemical-chemical (ECEC) mechanism (see supplementary information for details surrounding the determination of $E_{cat/2}$ and $\eta_{TOF/2}$). The PCET steps considered in this manuscript corresponds to concerted electron-proton transfer. Based on this detailed mechanistic analysis, we propose the design of improved ligand frameworks and explore their electronic structures with an energy decomposition analysis (EDA). This mechanistic analysis lays the foundation for further rational optimization of theoretically driven modifications of the ligand scaffold for improved catalytic activity.

METHODS

Computational Model. In this section we briefly explain the model, its assumptions and expected errors (see SI for more technical details and justifications). Density functional theory calculations for free energies, activation energies, reduction potential and the LOBA[51] oxidation state analysis were performed with the Q-Chem package[52] (version 5.3.0) using the ωB97X-D[54] functional with a mixed basis for the optimization and frequency calculations (def2-SVP basis for all main group elements, def2-TZVP basis set for Fe).[53] This functional was chosen based on our previous study and extensive functional screening (see SI reference [43]). In addition, we probed several other popular density functionals but no other functional yielded better agreement in both the predicted redox potentials and rates (see Table S7). Gibbs free energies (G) were used to compute reduction potentials and adiabatic spin gaps and are based on standard thermodynamic cycles.[54–56] Solvation energies were approximated by performing single point calculations applying the implicit C-PCM solvent model with the larger def2-TZVP basis for all elements[53] (see reference [57] more technical details). Reduction potentials are reported with an isodesmic scheme against the ferrocene/ferrocenium couple (Fc/Fc^+) used as an internal standard.[55,56,58] This method allows accurate predictions even at a modest level of theory with reported errors within approximately ~100 mV (~4 kcal/mol) of experimental values.[55] Of particular relevance to this work, this approach has yielded accurate calculated reduction potentials in several pyridine based electrocatalysts.[31,35,39] The RMSD of ωB97X-D for barrier heights is ~2 kcal/mol using gas phase high level wave function methods as the reference;[59,60] When comparing to experimental values, additional errors may arise from describing solvation by the implicit solvation model and other simplifications in the computational model versus experiment.

The calculation of free energies for protonation reactions with implicit solvent models results in expected deviations versus experimental values of ±3 pK_a units.[61] We tested our computational protocol for phenol (PhOH) with ωB97X-D yielding a pK_a of 24.6 which is 4-5 pK_a units too low.[62] While this is a large error, it also has a significant systematic component: calculated relative pK_a values are more reliable because of favorable error cancellation by removing the experimental free energy of the proton. Thus, calculated pK_a values should mainly be compared against each other.

We use PhOH as the main proton source for calculating reaction barriers involving protonation reactions as it was added to the reaction mixture in molar quantities for the CPE experiments. The concentration of other proton sources (H^+ and H_2CO_3) is negligible.[56] However, we report free energies of protonation reaction steps versus carbonic acid (H_2CO_3) because it is the strongest acid in solution and reprotonates phenolate (PhO^-) *via* complexation of CO_2 and OH^-. This approach was also used in a previous study of quaterpyridine based catalysts.[35] The calculated standard potential for the reduction reaction using carbonic acid is –1.28 V vs Fc/Fc^+; this is in good agreement with the experimental estimate of –1.27 V used in our previous study.[39] Matsubara[40] estimates the standard potential in wet CH_3CN depending on the mole fraction of water to be between 0.95 V and 1.63 V vs Fc/Fc^+.The highest predicted reduction potential is –1.83 V vs Fc/Fc^+ (η = 0.56 V) in our catalytic cycles (*vide infra*); this translates to a total reaction energy of –25.4 ($CO_2 + 2H_2CO_3 + 2e^- \rightarrow CO + H_2O + 2HCO_3^-$).

In contrast, the calculated standard potential using PhOH of –1.94 V vs Fc/Fc^+ is too negative. However, the calculated standard potential is lowered to –1.33 V by incorporating the effect of homoconjugation of phenol ins acetonitrile ($CO_2 + 6PhOH + 2e^- \rightarrow CO + H_2O + 2(PhO^- * 2PhOH)$).[42,43] The formation constant (K_f) for homoconjugation of PhOH in acetonitrile is very large ($\sim 10^{5.8}$)[41] and therefore we would expect significant formation even at very small concentrations of acid. This further complicates accurate determination of an unambiguous value of overpotential that would characterize the catalyst under these conditions (*i.e.,* $\eta_{TOF/2}$) as the value strongly depends on the concentration of the acid. Furthermore, here we report kinetics based on effective overpotentials (η_{eff}) and the corresponding applied potentials referenced to the Fc/Fc^+ couple across a wide potential range. We employ the energetic span model to predict the turnover frequency (TOF) based on our calculated catalytic cycles. This model identifies the key intermediates and transition states, which control the rate of catalysis (see the corresponding section for more detail).[62]

Experimental Methods. In this section we briefly outline the experimental techniques utilized to test our hypothesized mechanistic pathways. Additional details can be found in the supplementary information. Binding equilibria for CO_2 coordination and CO dissociation were investigated by cyclic voltammetry (CV) with varying scan rates (0.1 to 50 V/s). Catalytic stability was probed with multi-segmented CV experiments over one-hundred cycles as well as with long-term (1 h) preparative scale controlled potential

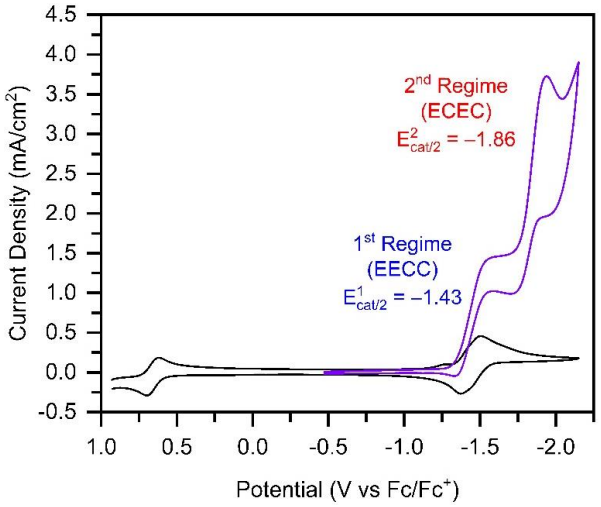

Figure 2. Electrochemical Characterization of ^{1}[Fe]$^{2+}$. Cyclic voltammograms of ^{1}[Fe]$^{2+}$ collected under Ar (black) and CO_2 (purple) with the addition of 1 M PhOH as a proton source. Cyclic voltammograms were collected with a scan rate of 100 mV/s in an electrolyte of 0.10 M $TBAPF_6$ dissolved in CH_3CN. The proposed two distinct mechanistic pathways for ^{1}[Fe]$^{2+}$ are designated by the potentials at which they reach half of the maximum catalytic current ($E_{cat/2}$) at −1.43 and −1.86 V vs Fc/Fc$^+$ and are labeled in blue and red, respectively. The first regime turns over from the 2$^+$ complex and undergoes a proposed EECC mechanism while the second regime at more negative potentials undergoes turnover from the 1$^+$ complex *via* an ECEC mechanism.

electrolysis (CPE) experiments taken across a range of applied potentials. Averaged Faradaic efficiencies for H_2 (FE_{H2}) and CO (FE_{CO}) production were determined from the one-hour CPE experiments, conducted in triplicate, with direct product detection by gas chromatography. The observed rate constants (k_{obs}) and turnover frequencies (TOF) were extracted from the averaged specific current densities for CO production (j_{CO}) over both short-term CPE experiments (5 min) conducted in a small CV cell and from long-term CPE experiments (1 hr) conducted in a large gastight PEEK electrolysis cell. We observed good agreement between rates obtained from both measurements. Kinetic isotope effects (KIE) were measured using 1 M solutions of phenol-H_6 and phenol-D_6 as the proton source. Observed rate constants for the KIE experiments were obtained using catalytic plateau current analysis despite the noncanonical catalytic behavior of [Fe]$^{2+}$ which makes this analysis inaccurate. This analysis was appropriate here because errors in rate determination are eliminated by taking the ratio of k_H/k_D.

RESULTS AND DISCUSSION

Observation of Two Distinct Overpotential-Dependent Regimes for Electrochemical CO_2 Reduction Catalyzed by [Fe(tpyPY2Me)]$^{2+}$. Electrochemical analysis of this molecular iron CO_2RR system exhibits two distinct catalytic regimes that are dependent on applied potential (Figure 2). Cyclic voltammograms collected under CO_2 atmosphere with the addition of 1 M phenol (PhOH), as a proton source, shows the formation of two catalytic waves. The first regime reaches a half-maximum catalytic current at a potential of −1.43 V vs Fc/Fc$^+$ ($E^1_{cat/2}$; η = 160 mV) and displays a canonical S-shaped wave indicative of pure kinetic conditions without substrate consumption.[43,44] At more negative applied potentials beyond −1.75 V vs Fc/Fc$^+$ (η = 480 mV), a second catalytic response is observed reaching a half-maximum catalytic current at a potential of −1.86 V vs Fc/Fc$^+$ ($E^2_{cat/2}$; η = 590 mV). This second catalytic regime shows peak-shaped behavior indicative of substrate consumption by the rate-determining step (Figure 2).[44]

The catalytic voltammogram clearly illustrates the formation of two catalytic waves with maximum current densities achieved at approximately −1.66 V vs Fc/Fc$^+$ (η = 390 mV) and −1.98 V vs Fc/Fc$^+$ (η = 710 mV). We attribute this behavior to the occurrence of two distinct catalytic regimes with disparate mechanisms. Building on this observation, we explore various reaction pathways for these two catalytic regimes in the presence of 1 M PhOH and 4-chlorophenol (Cl-PhOH) to probe the effect of the pK_a on the observed rates and to investigate the origin of selectivity of [Fe]$^{2+}$ for the CO_2RR relative to the HER (*vide infra*). The proposed mechanisms are in line with experimental kinetic data obtained from controlled potential electrolysis (CPE) experiments collected with direct product detection *via* gas chromatography. In order to compactly provide relevant information regarding the electronic structure of the proposed catalytic intermediates along the way, we introduce a naming scheme that incorporates the multiplicity (M, M= 2S+ 1), charge (C), and the identity of the sixth, axial ligand (X) on the iron center: ^{M}[Fe−X]^C; for example, ^{1}[Fe−CH_3CN]$^{2+}$ corresponds to the unreduced, hexacoordinated initial iron complex in the singlet state.

Low Overpotential Pathway. Figure 2 shows that the current density of the first catalytic regime reaches a plateau at approximately −1.66 V vs Fc/Fc$^+$ (η = 390 mV) with rates that are slower relative to the second catalytic regime. A mechanism for this first regime is illustrated in Figure 3 and presented in this section.

First, we propose two, sequential single electron reduction steps followed by the dissociation of CH_3CN to generate the catalytically active open-shell singlet, ^{1}[Fe]^0. CO_2 binding and subsequent protonation steps can then occur resulting in the loss of a water molecule and the formation of ^{1}[Fe−CO]$^{2+}$. Ligand exchange with exogenous CH_3CN and CO release closes the catalytic cycle. Interestingly, the formal oxidation state of the central metal does not change during catalysis. The following sections will expand upon these proposed individual elementary steps before we expand our discussion to include a proposed catalytic pathway for the second catalytic region that occurs at more negative potentials.

Reduction. The reduction pathway of ^{1}[Fe]$^{2+}$ was established in our initial report.[39] Variable temperature NMR and Mössbauer studies established that the starting ^{1}[Fe]$^{2+}$ complex is predominantly low-spin Fe(II) with a small population of thermally accessible spin excited states near room temperature that we attributed to the axial distortions engendered by the rigid tpyPY2Me ligand (Figure 4a). The first reduction of ^{1}[Fe]$^{2+}$ is ligand centered, with occupation of the tpy-π* orbital with almost no excess spin density on the metal center, yielding ^{2}[Fe−CH_3CN]$^+$, a ground state doublet

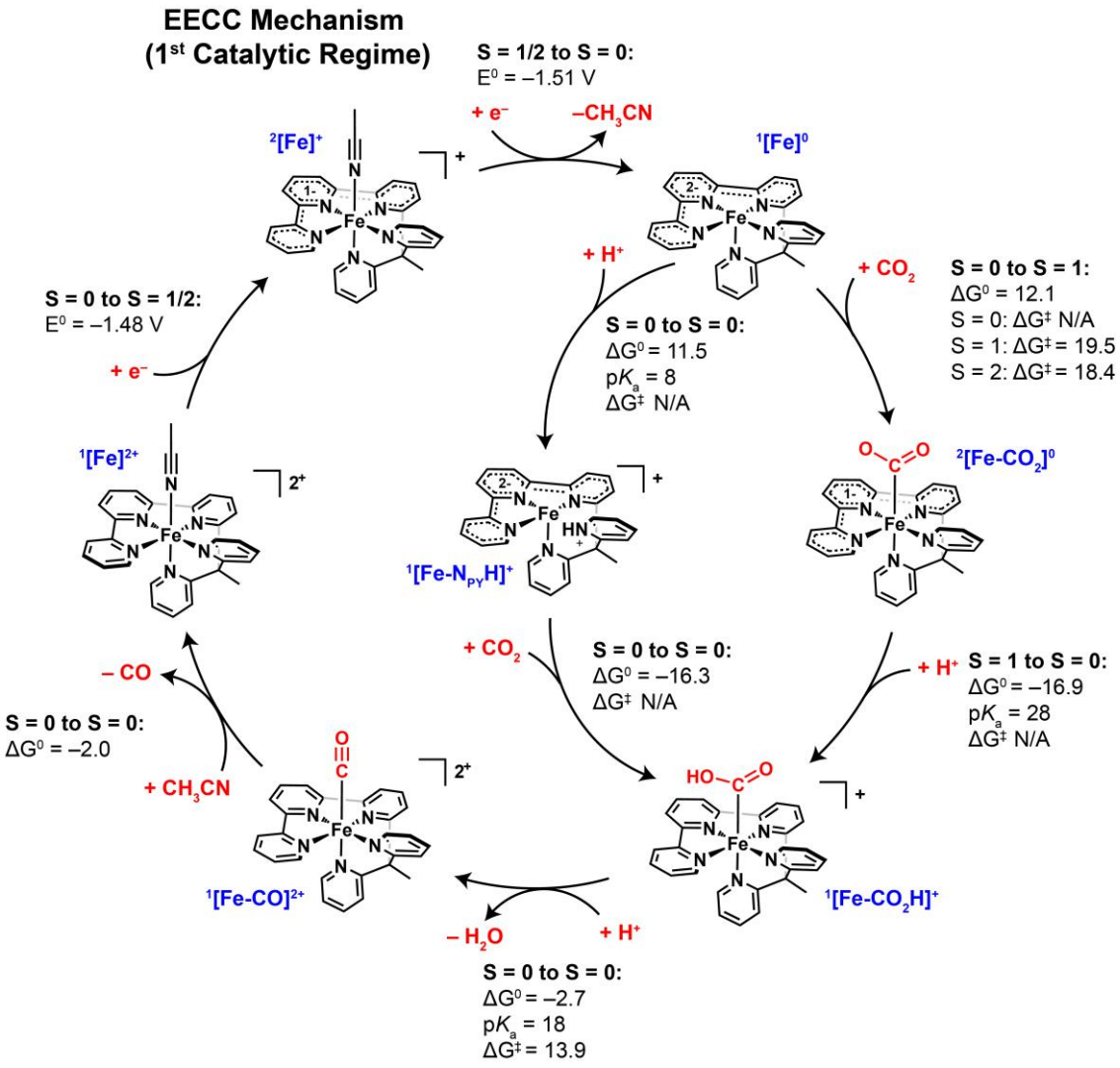

Figure 3. Proposed mechanistic pathways for the low overpotential regime. Starting from $^1[Fe]^{2+}$ (left side), we first propose two one-electron reduction steps followed by the dissociation of CH_3CN to generate the catalytically active open-shell singlet, $^1[Fe]^0$. CO_2 binding and subsequent protonation steps can then occur resulting in the loss of a water molecule and the formation of $^1[Fe–CO]^{2+}$. Ligand exchange with exogenous CH_3CN and CO release closes the catalytic cycle (outer pathway). Alternatively, direct protonation of the pyridyl arm in $^1[Fe]^0$ to give $^1[Fe–N_{PY}H]^+$ followed by CO_2 coordination and proton transfer was found to be a competitive pathway (inner pathway). All reaction and activation energies are given in units of kcal/mol and all reduction potentials are referenced to the computed Fc/Fc^+ couple.

composed of an low-spin Fe(II) center and a radical anion tpyPY2Me⁻ ligand (Figure 4b). The addition of a second electron occupies another tpy-π* orbital and induces a spin-state transition of the iron center from low-spin (S_{Fe} = 0) to intermediate-spin (S_{Fe} = 1) and ligand dissociation of the axially coordinated CH_3CN solvent molecule. This tetraradicaloid electronic configuration allows for strong exchange coupling of the two unpaired d electrons on the intermediate-spin iron center with the two electrons in the tpy-π* manifold, forming an overall open-shell singlet ground state, $^1[Fe]^0$ (Figure 4c). The open-shell singlet electronic structure was validated by synthesizing and isolating $^1[Fe]^0$ from the chemical reduction of $^1[Fe]^{2+}$ with decamethylcobaltocene and fully characterizing the resulting coordination compound by single-crystal X-ray crystallography, Mössbauer spectroscopy, X-ray absorption spectroscopy, and DFT and CASSCF calculations. Through these spectroscopic studies and with comparison to control complexes, we were able to attribute the catalysis of $^1[Fe]^{2+}$ for the CO_2RR at mild overpotentials to this antiferromagnetic complex. The predicted reduction potentials for the two reductions are −1.46 V and −1.51 V vs Fc/Fc^+, which are in good agreement with the experimental cyclic voltammetry data collected under argon atmosphere that show two closely spaced one-electron reduction waves centered at −1.43 V vs Fc/Fc^+. The exchange-coupling shifts the second reduction wave positive by a remarkable 640 mV relative to $[Zn(tpyPY2Me)]^{2+}$ which employs the same redox-active tpyPY2Me ligand, but contains a Zn(II) metal center that is unable to participate in stabilization through antiferromagnetic coupling.

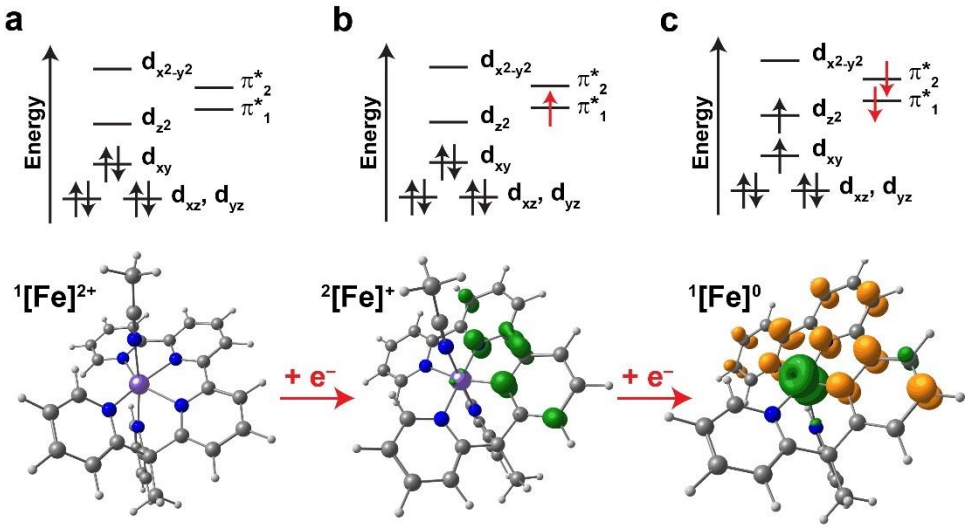

Figure 4. Spin densities and schematic MO diagrams: (a) unreduced complex $^1[Fe–L]^{2+}$ exhibiting no spin density; (b) singly reduced complex, $^1[Fe–L]^{2+}$, exhibiting spin density solely in the tpy ligand; (c) doubly reduced complex, $^1[Fe–L]^{2+}$, exhibiting spin density on both the metal center and the tpy moiety of the tpyPY2Me ligand in an exchange coupled state.

CO_2 Binding. CO_2 coordination occurs after $^1[Fe]^{2+}$ has been reduced by two electrons and the iron center has undergone a spin-state transition and subsequent ligand dissociation of the axially bound solvent molecule. The binding of CO_2 under standard conditions is endergonic and remains on the singlet surface yielding $^1[Fe–CO_2]^0$. We attempted to stabilize the CO_2 adduct with the addition of either explicit water molecules or electrolyte ($TBAPF_6$) but the binding remains endergonic with a free energy of +12.1 kcal/mol (ΔH = ~4 kcal/mol). The addition of an explicit phenol lead to direct protonation of the CO_2 moiety. The CO_2 ligand is bound *via* the carbon atom with an angle of 124º (Figure S1a). This structure is indicative of a closed-shell highly reduced CO_2 moiety and a low-spin singlet Fe(II) center with a neutral tpyPY2Me ligand. The LOBA analysis indicate that the two excess electrons are stabilized in a delocalized molecular orbital (MO), which mainly consists of the CO_2 π* orbitals but also has significant contribution from the Fe-$3d_{z^2}$ (40%) and some contribution from the tpy π* (see Figure S2).

The endergonic binding can be rationalized by the high stability of $^1[Fe]^0$, attributed to its antiferromagnetically coupled electronic structure, which yields a positive reduction potential but consequently at the cost of sluggish CO_2 binding. This prediction is in line with experimental findings as high concentrations of PhOH are required to observe CO_2 binding and subsequent catalysis. In order to probe the binding of CO_2, we attempted to measure the equilibrium constants for CO_2 binding (K_{CO_2}), based on the potential shift of the ligand reduction wave under Ar and CO_2 atmosphere (Figure S3). Under an Ar atmosphere, without the addition of PhOH as a proton source, there is no shift in the ligand reduction waves centered at −1.43 V vs Fc/Fc^+ (Figure S3a). When PhOH (1 M) is added, a catalytic wave is formed; however, a reversible couple could not be observed even when the experiment was performed with fast scan rates up to 50 V/s (Figure S3b,c). Taken together, these results suggest that CO_2 binding and thus catalysis is hampered when the system is proton limited. Interestingly, the higher spin-state surfaces [triplet ($^3[Fe]^0$) and quintet ($^5[Fe]^0$)] both exhibited much higher barriers for CO_2 binding that would effectively prevent catalysis. Thus, the open-shell singlet electronic structure of $^1[Fe]^0$ is key not only to decrease the overpotentials required for catalysis but also to facilitate CO_2 binding even though it is thermodynamically difficult. We further investigated an alternative pathway of CO_2 binding to a singly reduced intermediate ($^2[Fe]^+$). This pathway results in an even more endergonic CO_2 binding (14.1 kcal/mol) making it an unlikely intermediate.

Protonation. In a first scenario, the first protonation of $^1[Fe–CO_2]^0$ is barrierless and strongly exergonic (−16.9 kcal/mol) yielding the carboxyl intermediate, $^1[Fe–CO_2H]^+$ (Figure S1b). This intermediate can be best described as a CO_2H^- moiety coordinated to the Fe(II) center with the neutral tpy ligand framework. The second proton transfer step is exergonic (−2.7 kcal/mol) but with a barrier of 13.9 kcal/mol as it is coupled to the cleavage of the C–O bond and results in the loss of water and the formation of the carbonyl intermediate ($^1[Fe–CO]^{2+}$) (Figure S1c). The transition state geometry is depicted in Figure S5. The influence of explicit solvent molecules added to the transition state geometry was probed, but we were unable to find lower barriers with the addition of exogenous water molecules. In a second scenario, $^1[Fe]^0$ is protonated at one of the pyridine arms yielding a pyridinium intermediate, $^1[Fe–N_{PY}H]^+$ (Figure S1d). The calculated pK_a of 8 is quite acidic (versus a calculated pK_a of 16 for H_2CO_3); thus, the free energy of protonation coupled to carbonic acid is 11.5 kcal/mol. Previous experimental work by Matsubara shows that the pK_a of the reaction mixture is significantly lower with the addition of water. The experimental pK_a for CO_2 saturated water-acetonitrile mixtures can range from 7.8 to 16.8 where we would expect the addition of molar quantities of PhOH to further acidify the solution thus making this intermediate competitive.[40] The binding of CO_2 to $^1[Fe–N_{PY}H]^+$ is very exergonic

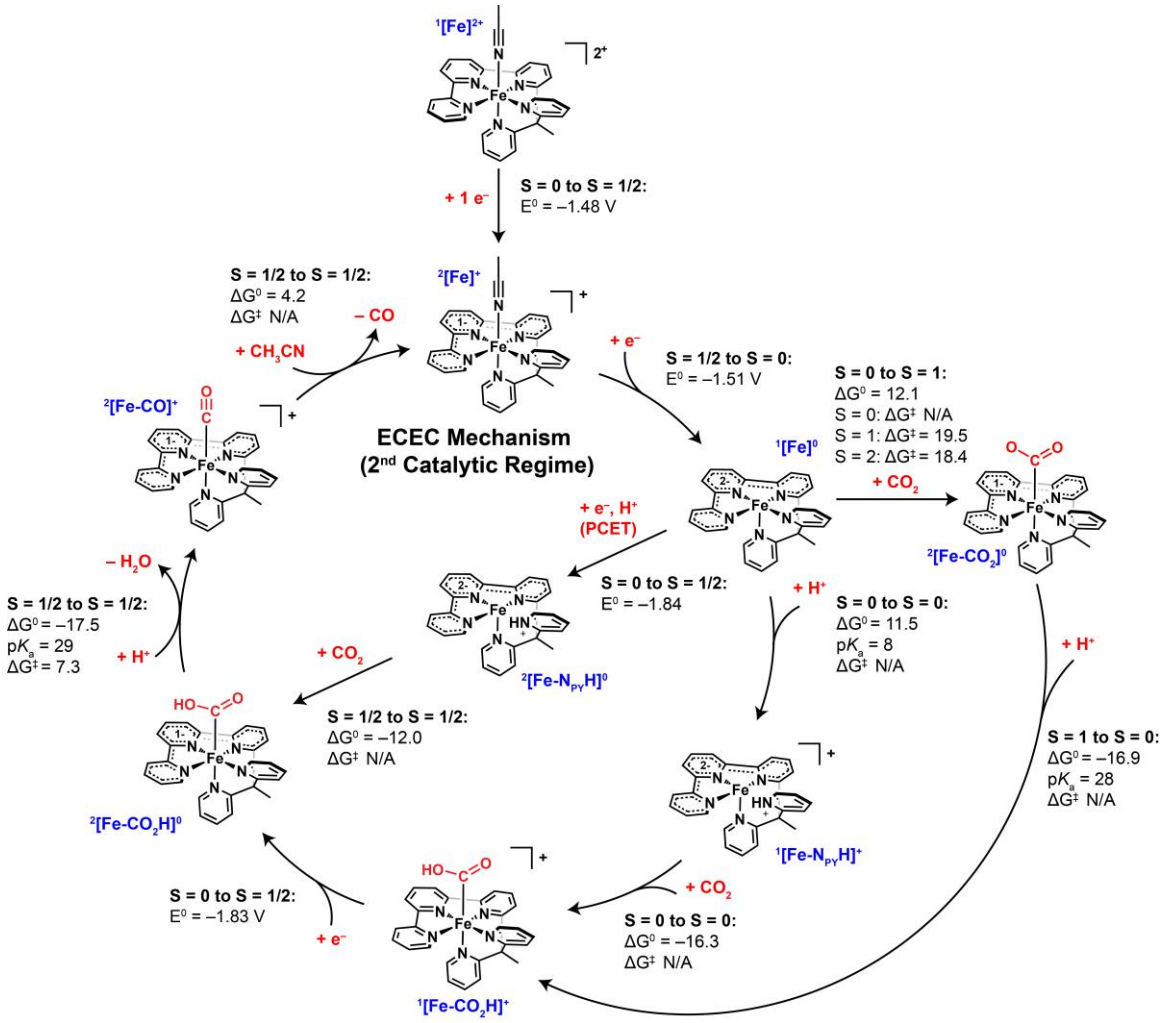

Figure 5. Proposed mechanistic cycles for the high overpotential regime. The high overpotential catalytic regime turns over from ^{2}[Fe]$^+$ following an initial induction period. Single-electron reduction of ^{2}[Fe]$^+$ gives the catalytic resting state, ^{1}[Fe]^0. Following formation of ^{1}[Fe]^0, the pathway diverges in three directions. CO_2 binding can occur first followed by protonation to give ^{1}[Fe–CO_2H]$^+$ (outer pathway) or protonation-first can occur followed by CO_2 coordination (inner pathway). The ^{1}[Fe–CO_2H]$^+$ intermediate can then be further reduced to ^{2}[Fe–CO_2H]^0 and following the final protonation step and loss of water generates the carbonyl complex, ^{2}[Fe–CO]$^+$ which regenerates ^{2}[Fe]$^+$ following ligand exchange. We additionally explore the possibility of overcoming the high energy barriers associated with either CO_2 binding or protonation of ^{1}[Fe]^0 by undergoing a PCET pathway to generate ^{2}[Fe–N_{PY}H]^0 (center pathway). All reaction and activation energies are given in units of kcal/mol and all reduction potentials are referenced to the computed Fc/Fc$^+$ couple.

(−16.3 kcal/mol) and directly yields a carboxy intermediate, ^{1}[Fe–CO_2H]$^+$ (Figure S1b), by skipping the high energy CO_2 adduct. This adduct is achieved by a simultaneous intramolecular proton transfer from the pyridinium and electron transfer from the tpy upon binding of CO_2 to form CO_2H^-. The second protonation proceeds as described above, see Figure 3 (outer pathway).

CO Release. CO release from ^{1}[Fe–CO]$^{2+}$ is exergonic and barrierless which can be attributed to the relatively high oxidation state of the iron center, which limits backbonding interactions. In addition, the low solubility of CO in CH_3CN promotes removal of CO from solution and into the gas phase. In order to further probe CO coordination and release, CVs of ^{1}[Fe]$^{2+}$ were collected under CO atmosphere and compared to data collected under Ar atmosphere. The addition of CO results in the formation of very small reductive features at −0.59 and a quantitative reductive wave at −1.23 V vs Fc/Fc$^+$. Additionally, the reversibility in the ligand reduction waves centered at −1.43 (Figure S6a) are lost at slower scan rates of 100 mV/s. We tentatively assign the new reduction wave at −1.23 V vs Fc/Fc$^+$ to the reduction of an Fe(II)-carbonyl species (^{1}[Fe–CO]$^{2+}$). This value agrees well with the predicted reduction potential of −1.18 V vs Fc/Fc+, supporting this assignment. We do note that attempts to spectroscopically characterize the waves at −0.59 and −1.23 V vs Fc/Fc$^+$ have been unsuccessful to date. Multi-segmented CV data collected under CO_2 atmosphere with the addition of 1 M PhOH, do not show any significant changes or the formation of new reductive features that could be attributed to the buildup of iron carbonyl species in the voltammograms across one-hundred cycles (Figure S6). Taken together, these data support the computational findings that CO binding is weakly endergonic by 2 kcal/mol and barrierless and thus we do not observe the

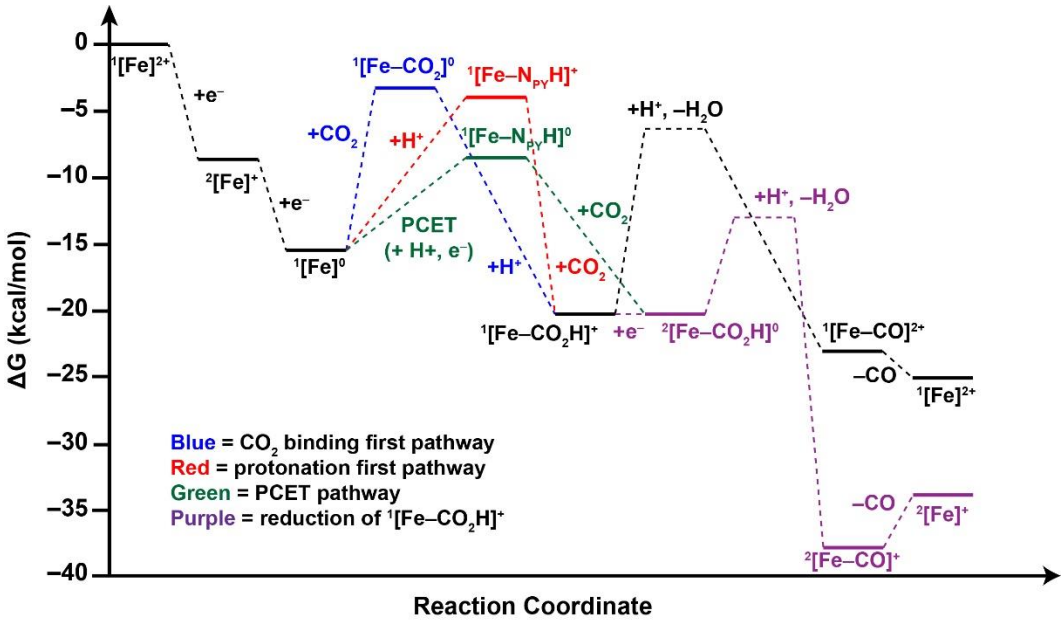

Figure 6. Free energy landscape for the low overpotential (Figure 3) and high overpotential (Figure 5) CO_2RR regimes. Colors signify different possible pathways that were proposed in the catalytic cycles shown in Figures 3 and 5. From the doubly reduced ^{1}[Fe]^0 intermediate, the blue line signifies the CO_2 binding first pathway, the red line denotes the protonation first pathway, and the green plots the PCET pathway. The purple line indicates the pathway where the ^{1}[Fe-CO_2H]$^+$ intermediate is further reduced in the high overpotential regime (refer to Figure 5). For the reduction steps, a potential of −1.8 V vs Fc/Fc$^+$ is applied; for the protonation steps, PhOH is used to estimate barriers and carbonic acid for free energies (see main text for justification); solid lines correspond to intermediate states and dashed lines to transition states.

accumulation of iron carbonyl species under electrocatalytic conditions. Further reduction of an iron carbonyl intermediate ^{2}[Fe–CO]$^+$ to ^{1}[Fe–CO]^0 can be eliminated based on the predicted redox potential which is more negative than −2.0 V vs Fc/Fc$^+$. A similar Fe(II)-carbonyl species equipped with a comparable terpyridine and pyridyl-N-heterocyclic carbene based ligand system was synthesized and structurally characterized by ^{1}H NMR and single crystal X-ray diffraction by Miller and coworkers.[63] Chemical reduction with two equivalents of decamethylcobaltocene resulted in the dissociation of the pyridine ligand and the formation of a pentacoordinate, low-valent iron carbonyl complex that was unfortunately shown to undergo rate limiting endergonic release of CO. The hemilability of the pyridyl arm to generate a stable 18-electron complex may be a defining feature to explain the difference in catalytic activity and speaks to the potential advantages engendered by utilizing a homoleptic tpyPY2Me ligand system.

High Overpotential Pathway. The application of more reducing potentials beyond −1.7 V vs Fc/Fc$^+$ results in the formation of a second catalytic wave. A mechanism for this high overpotential regime is illustrated in Figure 5 and presented in detail in this section. Here we investigate three potential pathways and found two to be aligned with experimental findings.

In all three cases, the initial reduction steps are identical in redox potential and electronic structure to what we presented for the low overpotential pathway discussed above. However, the first electron transfer is off-pathway; where at more reducing potentials, we find that there is enough driving force to reduce the carboxy intermediate (^{1}[Fe–CO_2H]$^+$) with a predicted redox potential of −1.83 V vs Fc/Fc$^+$ (*vide infra*). This observation results in catalytic turnover occurring from the singly reduced, iron complex (^{1}[Fe]$^+$) rather than turnover from the unreduced ^{1}[Fe]$^{2+}$. The three mechanistic pathways explored below diverge following the formation of the ^{1}[Fe]^0 catalytic resting state.

The proposed mechanism is depicted in Figure 5. In the first two scenarios, from the ^{1}[Fe]^0 intermediate, CO_2 coordination (Figure 5; outer cycle) or protonation (Figure 5; inner cycle) can occur first as discussed above for the low overpotential regime. Both pathways are uphill by approximately 11 kcal/mol and barrierless. The two pathways converge at the formation of the CO_2H adduct, ^{1}[Fe–CO_2H]$^+$, that can be further reduced at a calculated applied potential of −1.83 V vs Fc/Fc$^+$ yielding ^{2}[Fe–CO_2H]^0 where the electron populates one of the low-lying tpy-π* orbitals. The second proton transfer step to lose water and yield the carbonyl intermediate, ^{2}[Fe–CO]$^+$, is strongly exergonic by −17.5 kcal/mol (Figure S7). Moreover, the activation barrier for the second protonation is 7.3 kcal/mol, which is 4 kcal/mol lower than the barrier for the C–O bond cleavage step in the low overpotential regime. The CO release becomes endergonic by 4.2 kcal/mol due to the excess electron density that is transferred from the tpy-π* orbital to the Fe–CO moiety thus strengthening the backbonding to the CO ligand. Hence, the additional reductive event significantly lowers the barrier of the second protonation at the cost of more difficult CO release. Therefore, the second protonation is not as critical as in the low overpotential regime. Depending on the pathway, either the addition of CO_2 (12.1 kcal/mol) or the protonation of ^{1}[Fe]^0 (11.5 kcal/mol) become critical

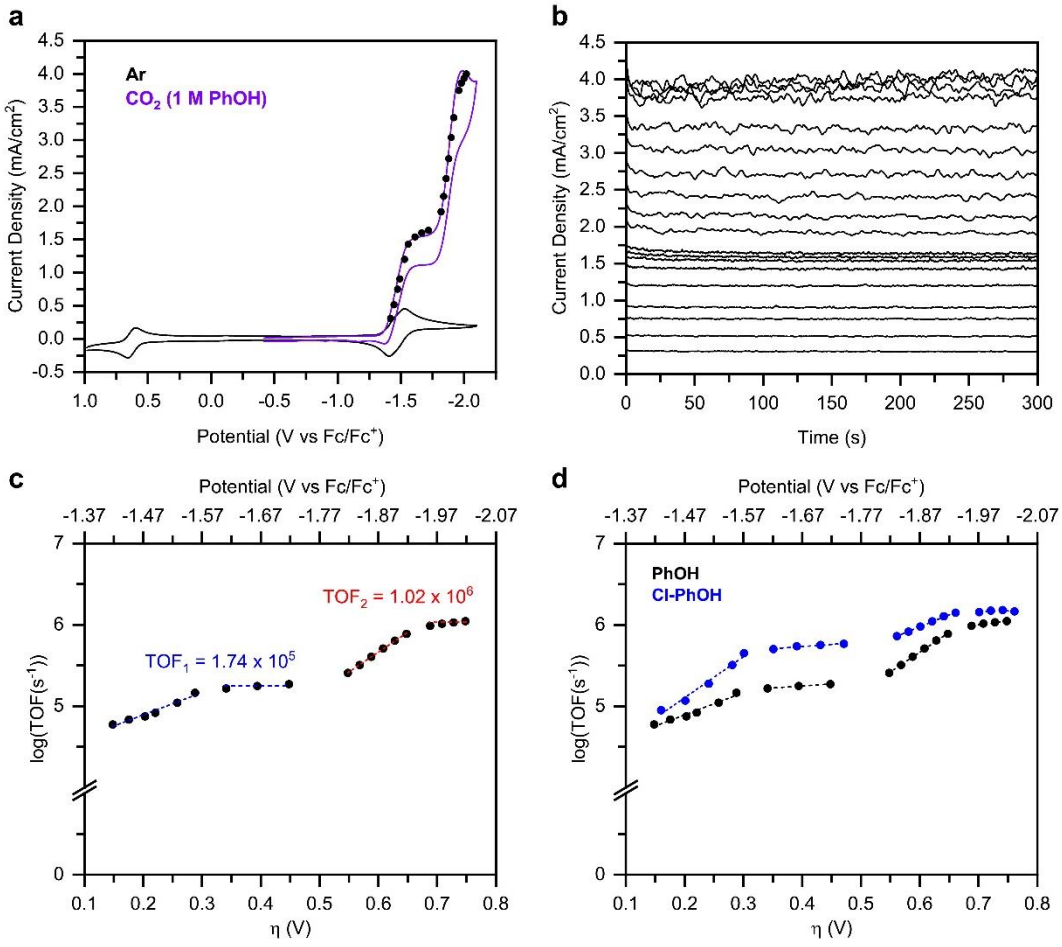

Figure 7. Kinetic analysis of ^{1}[Fe]$^{2+}$ (a) Cyclic voltammograms of ^{1}[Fe]$^{2+}$ in the absence (black) and presence (purple) of CO_2 with 1 M PhOH. Average current densities extracted from the short-term controlled potential electrolysis experiments (b) are overlayed on the catalytic CV (black dots) (c) Catalytic Tafel plot for ^{1}[Fe]$^{2+}$ obtained from the short-term CPE experiments with 1 M PhOH. (d) Comparison of catalytic Tafel plots obtained with 1 M PhOH or Cl-PhOH. CPE and CV experiments were collected in an electrolyte of 0.10 M $TBAPF_6$ dissolved in acetonitrile.

steps as well. Unfortunately, it is not possible to distinguish those two pathways computationally due to the small relative energy difference of 0.6 kcal/mol and the error associated with the predictions of protonation and CO_2 addition. It is possible that both channels are populated.

In a third scenario, following the formation of ^{1}[Fe]^0, a proton coupled electron transfer (PCET) pathway is possible where one of the pyridyl arms is protonated yielding ^{2}[Fe–N_{PY}H]^0. The additional electron is localized in the pyridinium moiety; thus, the electronic structure can be described as a doubly reduced tpy-π* moiety coupled to the intermediate spin iron center and a singly reduced pyridinium; this structure is summarized in the spin density plot in Figure S8. The reduction potential is acid dependent; using H_2CO_3 the calculated reduction potential is –2.14 V vs. Fc/Fc$^+$. However, taking non-standard concentrations into account using a similar approach to Song and coworkers,[55] we compute a shift by 0.3 V resulting in a potential of –1.84 V. For reference using H$^+$ the computed reduction potential is –1.17 V vs Fc/Fc$^+$. Next, CO_2 can bind to ^{2}[Fe–N_{PY}H]^0 to directly yield ^{2}[Fe–CO_2H]^0 in an intramolecular proton and electron transfer step with a free energy of −12.0 kcal/mol and thus also "skipping" the high energy CO_2 adduct intermediate. The role of proton transfer during catalysis was examined by measuring the H/D kinetic isotope effects in both catalytic regimes using C_6H_5OH (PhOH-H_6) or C_6D_5OD (PhOH-D_6) as the proton source (Figure S9). Experimentally, normal primary H/D kinetic isotope effects were observed under both catalytic regimes (k_H/k_D of 1.59 and 1.22, respectively), suggesting that proton transfer is involved in the rate determining step, thus supporting the protonation-first pathways, and excluding the CO_2-first mechanism.

Kinetic Analysis of Proposed Mechanistic Pathways. The free energy landscape summarizing the total catalytic cycle is depicted in Figure 6. Following elucidation of the possible reaction pathways for CO_2 reduction across both potential-dependent regimes, we next sought to compare experimentally determined kinetic data against computationally derived turnover frequencies (TOFs) obtained from the energetic span computational model developed by Kozuch and coworkers.[64] The energetic span model was employed to identify key intermediates and transition states, which control the rate of catalysis. This model connects the free

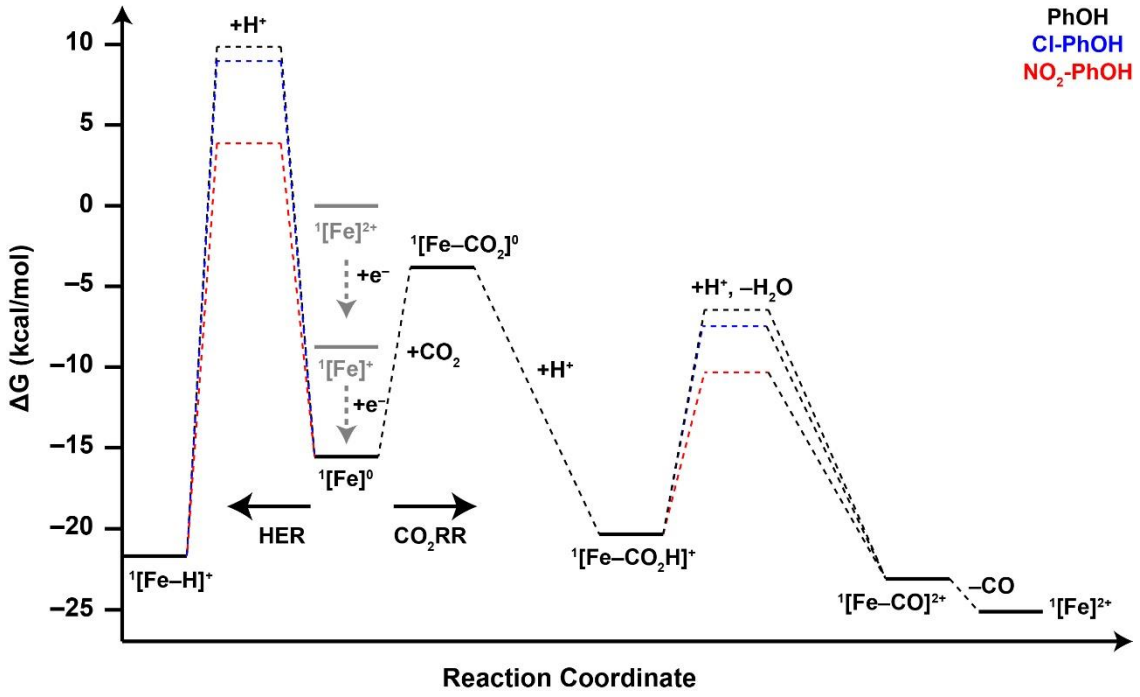

Figure 8. Free energy landscape of the low overpotential regime for CO_2RR and HER pathways. For the reduction steps, a potential of –1.8 V vs Fc/Fc$^+$ is applied. For the protonation steps, PhOH is used to estimate barriers and carbonic acid for free energies (see main text for justification). Solid lines correspond to intermediate states and dashed lines to transition structures. Black, blue, and red lines denote the uses of PhOH, Cl-PhOH, and NO_2-PhOH, respectively.

energy landscape of the DFT based catalytic cycles with the experimentally measured TOFs using Eyring transition state theory. The model identifies TOF-determining transition states (TDTS) and the TOF-determining intermediates (TDI) and computes rates based on the energetic span of these two states.[64] Often there are various intermediates with a significant influence on the catalytic rates. This progression can be quantified in this model by the degree of TOF control (denoted as X_{TOF}),[65] which describes how the TOF varies by a small change in energy of that intermediate or transition state. The range of X_{TOF} is between 0 and 1, where 0 denotes that the species has no influence on the TOF and 1 denotes that the species solely controls the TOF.[66,67] The results from the energetic span calculations are presented in Tables S1 – S6.

Experimental kinetic parameters were obtained from variable controlled potential (CPE) experiments as described by Savéant and co-workers.[49,50] Short-term (5 min; Figure 7) and long-term (1 h; Figure S10 and S11) CPE experiments were performed where the products (CO and H_2) were detected and quantified by gas chromatography for the long-term CPE experiments conducted in an air-tight electrochemical cell. The observed rate constants (k_{obs}) at each applied potential were extracted from the average specific current densities taken across the entire electrolysis experiment and were then compared to the computed rates obtained from the energetic span model (Figures S10 and S11 and Tables S1–S6). To further probe the influence of the proton transfer step on the observed rates, PhOH (see Figure 7), and Cl-PhOH (see Figures S10 – S12), which is approximately one pK_a unit more acidic (in water), were utilized.

First, we explored the kinetics of the low overpotential regime (potential window of −1.40 – −1.75 V vs Fc/Fc$^+$). Short-term CPE data collected at applied potentials between −1.42 and −1.72 V vs Fc/Fc$^+$ overlay closely with the voltammogram collected under CO_2 atmosphere with 1 M PhOH (Figure 7a). Current densities were stable across the entire short-term electrolysis (Figure 7b) and long-term electrolysis (Figures S10 and S11) and reached a plateau at ca. −1.66 V vs Fc/Fc$^+$ with an average current density of 1.53 mA/cm^2 which corresponds to a TOF of 1.74 x 10^5 s^{-1} (Figure 7c). When the more acidic, Cl-PhOH was added as the proton donor, the maximum TOF of the first catalytic regime increased to 5.50 x 10^5 s^{-1}, a three-fold increase in observed rate relative to the data obtained with PhOH as the proton source (Figure 7d) without loss of product selectivity (Figure S13). Analysis of this catalytic regime with the energetic span model shows that the catalytic rate is solely controlled by the second protonation step (C–O bond cleavage to release water) as the key rate-limiting intermediate and transition state are both associated with the second protonation. The carboxy intermediate, ^{1}[Fe–CO_2H]$^+$, is the TDI and the second protonation barrier is the TDTS both with X_{TOF} values close to 1. Based on this analysis, a TOF of 400 s^{-1} is predicted. This value is slower than the experimentally determined TOF of 1.74 x 10^5; however, this translates to an energy difference of ~3.5 kcal/mol which is still within acceptable agreement. Furthermore, when Cl-PhOH is utilized as the acid source, the barrier is lowered by 1.1 kcal/mol which translates to a rate increase by one order of magnitude. The stronger acid lowers the TDTS, leading to an increase in the importance of the CO_2 binding step. This shift is illustrated by the change in the degree of TOF control: Indeed, the X_{TOF} of both the TDI (^{1}[Fe–CO_2H]$^+$) and TDTS

decreases from 0.97 to 0.82 and the CO_2 binding step is increasingly important for the rate as the X_{TOF} increases to 0.16 from 0.03. Distinction between the protonation first or CO_2 binding first pathways by this kinetic analysis was not possible because both options occur before the rate determining protonation step.

Application of more negative onset potentials between −1.81 and −2.01 V vs Fc/Fc^+ allowed us to probe the kinetics of the second, high overpotential regime. Tight correlations were observed between the averaged current densities from the CPE experiments and the cyclic voltammograms collected under CO_2 atmosphere with PhOH (Figure 7a) or Cl-PhOH (Figure S12a). Peak current density of 4.0 mV/cm^2 was reached at −2.01 V vs Fc/Fc^+ which corresponds to a maximum TOF of 1.05 x 10^6 s^{-1}. Addition of 1 M Cl-PhOH as the proton source results in a smaller rate enhancement with a maximum TOF of 1.5 x 10^6 s^{-1}, representing only a 1.4-fold enhancement relative to PhOH, about half of what was observed in the low overpotential regime (Figure 7d and S13). Catalytic Tafel plots comparing the two acids are presented in Figure 7d. In addition, there is still a proton dependence on the rate limiting step as illustrated by the normal, primary H/D kinetic isotope effect.

Next, the energetic span model was applied to predict the rates for the three possible mechanistic pathways proposed for the high overpotential regime. These rates are then compared to the experimentally determined TOFs. The three pathways are given in Figure 5 and are illustrated in a free energy diagram (Figure 6) to allow for more direct comparison. From the $^1[Fe]^0$ catalytic resting state, the iron complex can either go through: (1) a CO_2 coordination first pathway to give the CO_2 complex ($^2[Fe–CO_2]^0$); (2) a protonation first pathway to generate the cationic pyridinium intermediate, $^1[Fe–N_{PY}H]^+$; or a PCET pathway to generate a similar neutral pyridinium species, $^2[Fe–N_{PY}H]^0$.

A TOF of 4000 s^{-1} is predicted for the CO_2 binding first pathway. The TOF is completely controlled by the CO_2 coordination step as the reduction of $^1[Fe–CO_2H]^+$ to $^2[Fe–CO_2H]^0$ lowers the (previously rate limiting) barrier for the second protonation by 6.6 kcal/mol from 13.9 to 7.3 kcal/mol. This shrinks the X_{TOF} for both $^1[Fe–CO_2H]^+$ and the transition state for the second protonation to 0. The CO_2 first pathway can be eliminated because CO_2 coordination is shown by the energetic span model to be entirely rate limiting and thus fails to explain the experimentally observed normal, primary H/D kinetic isotope effect and a large catalytic enhancement with the addition of more acidic proton donors.

Next, for the protonation first pathway, we predict a TOF that is almost 3 orders of magnitude slower than what we observed experimentally (11000 s^{-1}). Additionally, we find that the cycle is solely controlled by the first protonation of $^1[Fe]^0$ to give the pyridinium intermediate, $^1[Fe–N_{PY}H]^+$. The protonation first pathway would account for the primary kinetic isotope effect but not the rate enhancement upon addition of stronger acids as the energetic span model predicts the same rate regardless of if PhOH or Cl-PhOH are utilized as the proton source.

The TOF predicted for the PCET pathway of 1.4 x 10^7 s^{-1} resulted in the closest match to the experimentally measured value of 1.05 x 10^6 s^{-1} with the pathway being controlled by both the PCET step as well as the second protonation of $^2[Fe–CO_2H]^0$ as both have X_{TOF} coefficients close to 0.5. The *para*-chloro substituted PhOH, Cl-PhOH, lowers the barrier for the second protonation by 2.6 kcal/mol. However, only the PCET pathway is kinetically controlled by this transition state increasing the TOF from 1.4 x 10^7 s^{-1} to 2.6 x 10^7 s^{-1}. This increase is smaller than the increase in the low overpotential regime despite a stronger effect on barrier lowering, which can be understood by the lower X_{TOF} of that step in the low versus high overpotential regime. Based on the experimental and computational findings, these data suggest that the PCET pathway is the more likely mechanism for the high overpotential regime.

Selectivity Versus HER. Achieving selectivity for CO_2 reduction over the reduction of protons to H_2 is critical. The HER is a competitive side reaction across a similar potential window to the CO_2RR and is highly dependent on the presence and strength of the proton source.[14] The generation of an iron hydride under reducing conditions in the presence of a proton donor can thus shift the catalyst selectivity away from CO production and toward the formation of H_2. It is therefore important to understand the kinetic and thermodynamic barriers associated with the protonation of the reduced iron center.

In our proposed pathway there are two critical intermediates through which the formation of a hydride is feasible (Figure 8 and S15). The first possibility is the direct protonation of the iron center of the doubly reduced intermediate, $^1[Fe]^0$ (Figure 8 and S16a). The other possibility is the rearrangement of the pyridinium intermediate, $^1[Fe–N_{PY}H]^+$, to a metal hydride (Figure 8 and S16b). In both cases, high activation barriers prevent these side reactions and explain the high product selectivity for CO_2 reduction to CO that is observed experimentally. The direct formation of a hydride $^1[Fe–H]^+$ from $^1[Fe]^0$ albeit thermodynamically favorable with a free energy of −6.1 kcal/mol, is kinetically inhibited with a high activation barrier of 24.5 kcal/mol. The rearrangement of $^1[Fe–N_{PY}H]^+$ to $^1[Fe–H]^+$, is more exergonic (−17.5 kcal/mol); however, this pathway is also inhibited by a larger activation barrier of 21.4 kcal/mol. In both cases, the high barriers can be rationalized by the electronic structure of $^1[Fe]^0$: the metal center stabilizes the two ligand reductions through antiferromagnetic coupling and thus the metal center remains Lewis acidic. This feature is illustrated by the coordination of acid (*e.g.*, PhOH or H_2CO_3) to $^1[Fe]^0$ in which the acid prefers to bind *via* the oxygen atom to the iron center which then facilitates the protonation of the pyridyl arm, but blocks the metal center from protonation (see Figure S17). Therefore, the formation of a metal-hydride is prohibited by steep kinetic barriers ultimately shutting down pathways to hydrogen production. The difference between the rate limiting transition state in CO_2RR and the barrier for hydride formation is ~10 kcal/mol which implies that $^1[Fe]^{2+}$ should remain selective for the CO_2RR even when stronger acids are used as proton donors. Indeed, selectivity is achieved by using 4-nitrophenol (NO_2-PhOH), an even stronger acid (two pK_a units stronger than Cl-PhOH), with a barrier of 19.3 kcal/mol for the formation of a hydride. We explored this possibility, and, in all cases, we do not detect any hydrogen formation experimentally.

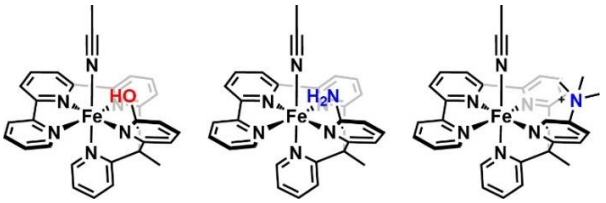

Figure 9. Chemical structures of second-sphere functionalized polypyridyl catalysts for improved performance based on our mechanistic understanding.

However, NO_2-PhOH was also redox-active at the potentials applied, which also prevented the formation of CO.

Rational Catalyst Design Driven by Mechanistic Insights. Based on the mechanistic studies we identified several critical intermediates and transition states that directed us to propose improved ligand designs that ideally stabilize several critical intermediates. The key takeaways from the kinetic analysis are: first, the low overpotential regime is solely controlled by the second protonation step, even when strong acids are used. Thus, modifications must either lower the energy of the transition state or decrease the stability of the carboxy intermediate. Second, the high overpotential regime is mainly controlled by either the CO_2 adduct or the formation of the pyridinium intermediate, especially when stronger acids are used as the proton source. Thus, an optimal modification should have a positive effect on both the CO_2 binding and second protonation. On the basis of our detailed mechanistic investigation, we propose rationally designed synthetic modifications to the tpyPY2Me ligand to further increase the catalytic performance of the iron complex. Synthetic modification to the pyridine moiety is the most promising for two reasons: first, it does not affect the initial reduction potentials and the crucial antiferromagnetic coupling of $^1[Fe]^0$; second, substituents can affect all critical intermediates by stabilizing the bound CO_2 adduct, increasing the pK_a of the pyridine itself for protonation and PCET, and then stabilizing the transition state for the second protonation (Figure 9 shows the investigated candidates). In order to gain quantitative insights, we use the absolutely localized MO energy decomposition analysis with continuum solvation (ALMO-EDA(solv))[67] (see SI for a short introduction and a more detailed review is also available[68]) to understand how a specific modification stabilizes the reduced CO_2 adduct. We employ a difference-of-differences-approach where we compare the change in interaction energy and EDA terms using the unsubstituted tpyPY2Me ligand as the reference. We investigate hydrogen bonding (–OH and–NH_2) and ionic stabilization (–$N(CH_3)_3^+$) as both moieties are known to facilitate CO_2 binding in other CO_2RR catalysts (see Figure 9).[12,19,22,30,31,69] The EDA decomposition of that change in interaction energy is crucial for understanding the exact stabilization pathway as substituents affect the reduced CO_2 not only directly *via* a non-covalent interaction but also indirectly through substituent effects. Both pathways often have distinct EDA fingerprints and thus can be distinguished by an EDA scheme. We recently showed the viability of this approach for an iron tetraphenylporphyrin catalyst.[67] The chosen reference fragmentation of the complex is a doubly reduced CO_2^{2-} and an unreduced catalyst. This fragmentation is more suitable for this type of complex as the O–C–O bond angle of 124º indicates a transfer of both electrons into the CO_2 moiety. The alternative choice, a neutral but bent CO_2 fragment and a doubly reduced metal complex will be solely dominated by the geometry distortion term as discussed elsewhere.[67,68] Thus, this interaction energy decomposed by the EDA scheme corresponds to the stabilization of the doubly

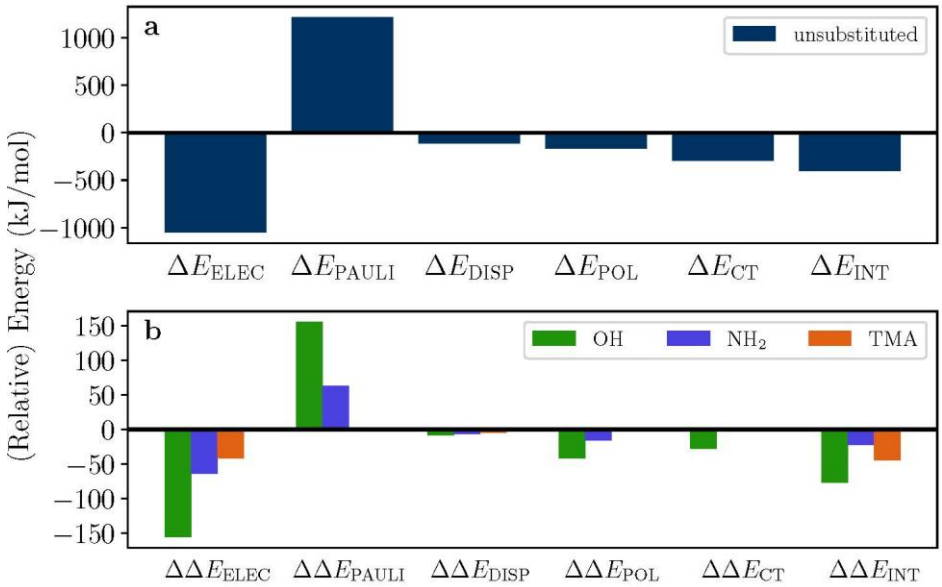

Figure 10. ALMO-EDA (solv) results for CO_2 adduct $^1[Fe–CO_2]^0$: (a) the unsubstituted adduct; (b) differential ALMO-EDA (solv) results for three different substituents: –OH (green), –NH_2 (blue), and –$N(CH_3)_3^+$ (TMA; orange). Energies are reported in kJ/mol.

reduced CO_2^{2-} dianion by the unreduced catalyst. It is important to point out that this is just a part of the total free energy of CO_2 addition. The EDA results for the unsubstituted complex are given in Figure 10a and shows that the attractive interactions are dominated by electrostatic interactions with significant charge transfer contributions. The short Fe–C bond distance of 2.05 Å rationalizes the high Pauli repulsion, and indicates that net binding energy results mainly from CT. The change in interactions energies as well as each EDA component for each substituent relative to the unsubstituted complex is depicted in Figure 10b. The *ortho*-hydroxy substituent (*o*-OH) strengthens the interaction by 77.1 kJ/mol (18.5 kcal/mol). The main driving force is additional favorable electrostatic interaction, which is also supplemented by favorable contributions from polarization and charge transfer, which are typical of a hydrogen bonding fingerprint.[70] The large increase in Pauli repulsion can be attributed to the repulsion of the diffuse lone pairs of the CO_2 moiety and the hydroxy group. Interestingly, this intermediate was not stable without freezing the hydroxy OH bond as it otherwise directly protonates the CO_2 moiety. The *ortho*-amino substituent has a much smaller stabilizing effect of −22.5 kJ/mol (5.4 kcal/mol). The favorable electrostatic interaction cannot overcome the additional Pauli repulsion of the amino substituent and the CO_2^{-2} moiety. Lastly, the charged trimethylanilinum (TMA) moiety had to be placed at the *meta* position due to the bulkiness of the group. The EDA results demonstrate how this group provides a purely electrostatic stabilization; however, the solvation screens most of the interaction to yield an overall stabilization of −44.6 kJ/mol (−10.7 kcal/mol). Moreover, the *ortho* hydrogen donating substituents have another advantage: They can stabilize the transition state for the second protonation step by forming hydrogen bonds. These interactions lower the transition state (see Figure S18) for the *o*-OH by 1.3 kcal/mol which translates to an order of magnitude faster TOF in the low overpotential regime (similar effect to the use of stronger acids).

CONCLUSIONS

In summary, inspired by the excellent observed catalytic performance of the molecular $[Fe(tpyPY2Me)]^{2+}$ system, we investigated the mechanistic pathways through which it electrochemically converts CO_2 into CO. Cyclic voltammograms collected under CO_2 atmosphere displayed the formation of two distinct catalytic regimes with $E^1_{cat/2}$ of −1.43 V vs Fc/Fc^+ ($\eta_{TOF/2}$ = 160 mV) and $E^2_{cat/2}$ −1.86 V vs Fc/Fc^+ ($\eta_{TOF/2}$ = 590 mV). For the low overpotential regime, the computed pathway shows that $^1[Fe]^{2+}$ first undergoes two, single-electron reduction steps to generate the five-coordinate open-shell singlet, $^1[Fe]^0$. From $^1[Fe]^0$, we show that the order of CO_2 addition or protonation is flexible and experimentally indistinguishable with both steps having comparable calculated barriers. We find that both CO_2 binding and protonation of the pyridine arm are feasible steps with similar endergonic free energies. In any case, the rate limiting step was found to be the second protonation step resulting in cleavage of the C–O bond with subsequent CO release being barrierless and exergonic. Analysis of the complete low overpotential regime revealed that catalysis is solely controlled by the carboxyl intermediate ($^1[Fe–CO_2H]^+$) and the transition state for the second protonation step. Consequently, the use of a stronger proton source, such as ClPhOH, resulted in a three-fold increase in the rate of catalysis without any loss in product selectivity. Computational analysis of the high overpotential regime shows a similar two initial electron transfer steps; however, at more reducing potentials, the first reduction is off-pathway, allowing for turnover from $^2[Fe]^+$ rather than $^1[Fe]^{2+}$ as is observed in the low overpotential regime. Following formation of the catalytic resting state, $^1[Fe]^0$, we computationally probed three mechanistic pathways and compared them to experimental kinetic data and results obtained from the energetic span model. From this analysis, we identified the PCET pathway of one of the pyridine arms as the most consistent mechanism. This intermediate readily binds CO_2 and rearranged into a singly reduced carbonyl intermediate. The additional electron greatly facilitates the second protonation step explaining the increased rates observed for the higher overpotential regime. Analysis of the cycle showed that both the PCET and the second protonation steps control the rate of catalysis. As such, similar to the low overpotential regime, the use of a more acidic proton source increases the rate of catalysis, but to a lesser degree. The stronger acid only lowers the barrier for the second protonation; however, this step has less influence on the turnover frequency and thus the effect of acid pK_a is lower.

Finally, the mechanistic insights gained from this study identified the pyridyl arms as promising targets for further optimization of the catalytic performance of this system. The pyridyl arms are not involved in stabilizing the excess electron density in the reduction events and thus any modifications should not alter the reduction potential of $^1[Fe]^{2+}$, which is already optimally matched to the standard redox potential for the conversion of CO_2. The introduction of hydrogen bond donors into the second coordination sphere can further greatly stabilize the CO_2 adduct and lower the transition state for the second protonation step, both of which are critical intermediates for fast catalysis. Moreover, we also expect that the substituent effects can help to stabilize the pyridinium intermediate; therefore, this synthetic modification has the potential to improve catalysis in all proposed cycles for both the low and high overpotential regimes.

ASSOCIATED CONTENT

Supporting Information. Supporting Information. Experimental and computational details, supplemental electrochemical and DFT geometry optimized atomic xyz coordinates is available free of charge via the Internet at http://pubs.acs.org.

AUTHOR INFORMATION

Corresponding Author

*Martin Head-Gordon – Department of Chemistry University of California, Berkeley, CA, 94720, USA; Chemical Sciences Division, Lawrence Berkeley National Laboratory, Berkeley, CA, 94720, USA. orcid.org/0000-0002-4309-6669; Email: mhg@cchem.berkeley.edu.

*Christopher J. Chang – Departments of Chemistry and Molecular and Cell Biology University of California, Berkeley, CA, 94720, USA; Chemical Sciences Division, Lawrence Berkeley

National Laboratory, Berkeley, CA, 94720, USA. orcid.org/0000-0001-5732-9497; Email: chrischang@berkeley.edu

Authors

Matthias Loipersberger – Department of Chemistry University of California, Berkeley, CA, 94720, USA. orcid.org/0000-0002-3648-0101.

Jeffrey S. Derrick – Department of Chemistry University of California, Berkeley, CA, 94720, USA; Chemical Sciences Division, Lawrence Berkeley National Laboratory, Berkeley, CA, 94720, USA. orcid.org/0000-0002-3879-2897.

Author Contributions

‡M.L. and J.S.D. contributed equally. CJC, and MHG conceptualized the project. JSD performed all experimental work. ML carried out all the computational work. ML and JSD analyzed the data and wrote the manuscript with input from CJC and MHG.

ACKNOWLEDGMENT

This work was supported by the U.S. Department of Energy, Office of Science, Office of Advanced Scientific Computing, Office of Basic Energy Sciences, via the Scientific Discovery through Advanced Computing (SciDAC) program (M.H.G.) and the Division of Chemical Sciences, Geosciences, and Bioscience of the U.S. Department of Energy at Lawrence Berkeley National Laboratory (Grant No. DE-AC02-05CH11231 to C.J.C.). J.S.D. thanks Chevron for a graduate fellowship. C.J.C. is a CIFAR Fellow.

REFERENCES

(1) Lewis, N. S.; Nocera, D. G. Powering the Planet: Chemical Challenges in Solar Energy Utilization. *Proc. Natl. Acad. Sci.* **2006**, *103*, 15729–15735.

(2) De Luna, P.; Hahn, C.; Higgins, D.; Jaffer, S. A.; Jaramillo, T. F.; Sargent, E. H. What Would It Take for Renewably Powered Electrosynthesis to Displace Petrochemical Processes? *Science* **2019**, *364*, eaav3506.

(3) Nguyen, V.-H.; Nguyen, B.-S.; Jin, Z.; Shokouhimehr, M.; Jang, H. W. Towards artificial photosynthesis- Sustainable hydrogen utilization for photocatalytic reduction of CO_2 to high-value renewable fuels. *Chem. Eng. J.* **2020**, *402*, 126184.

(4) Gust, D.; Moore, T. A.; Moore, A. L. Solar Fuels via Artificial Photosynthesis. *Acc. Chem. Res.* **2009**, *42*, 1890–1898.

(5) Appel, A. M.; Bercaw, J. E.; Bocarsly, A. B.; Dobbek, H.; DuBois, D. L.; Dupuis, M.; Ferry, J. G.; Fujita, E.; Hille, R.; Kenis, P. J. A.; Kerfeld, C. A.; Morris, R. H.; Peden, C. H. F.; Portis, A. R.; Ragsdale, S. W.; Rauchfuss, T. B.; Reek, J. N. H.; Seefeldt, L. C.; Thauer, R. K.; Waldrop, G. L. Frontiers, Opportunities, and Challenges in Biochemical and Chemical Catalysis of CO_2 Fixation. *Chem. Rev.* **2013**, *113*, 6621–6658.

(6) Sun, Z.; Ma, T.; Tao, H.; Fan, Q.; Han, B. Fundamentals and Challenges of Electrochemical CO_2 Reduction Using Two-Dimensional Materials. *Chem*, **2017**, *3*, 560–587.

(7) Verma, S.; Kim, B.; Jhong, H.-R. "Molly"; Ma, S.; Kenis, P. J. A. A Gross-Margin Model for Defining Technoeconomic Benchmarks in the Electroreduction of CO_2. *ChemSusChem* **2016**, *9*, 1972–1979.

(8) Kumar, B.; Llorente, M.; Froehlich, J.; Dang, T.; Sathrum, A.; Kubiak, C. P. Photochemical and Photoelectrochemical Reduction of CO_2. *Annu. Rev. Phys. Chem.* **2012**, *63*, 541–569.

(9) Long, C.; Li, X.; Guo, J.; Shi, Y.; Liu, S.; Tang, Z. Electrochemical Reduction of CO_2 over Heterogeneous Catalysts in Aqueous Solution: Recent Progress and Perspectives. *Small Methods* **2019**, *3*, 1800369.

(10) Razzak, S. A.; Ali, S. A. M.; Hossain, M. M.; deLasa, H. Biological CO_2 Fixation with Production of Microalgae in Wastewater – A Review. *Renew. Sustain. Energy Rev.* **2017**, *76*, 379–390.

(11) Elouarzaki, K.; Kannan, V.; Jose, V.; Sabharwal, H. S.; Lee, J.-M. Recent Trends, Benchmarking, and Challenges of Electrochemical Reduction of CO_2 by Molecular Catalysts. *Adv. Energy Mater.* **2019**, *9*, 1900090.

(12) Nichols, A. W.; Machan, C. W. Secondary-Sphere Effects in Molecular Electrocatalytic CO_2 Reduction. *Front. Chem.* **2019**, *7*, 397.

(13) Luo, Y.-H.; Dong, L.-Z.; Liu, J.; Li, S.-L.; Lan, Y.-Q. From Molecular Metal Complex to Metal-Organic Framework: The CO_2 Reduction Photocatalysts with Clear and Tunable Structure. *Coord. Chem. Rev.* **2019**, *390*, 86–126.

(14) Kinzel, N. W.; Werlé, C.; Leitner, W. Transition Metal Complexes as Catalysts for the Electroconversion of CO_2: An Organometallic Perspective. *Angew. Chem. Int. Ed.* **2021**, *60*, 11628–11686.

(15) Sun, L.; Reddu, V.; Fisher, A. C.; Wang, X. Electrocatalytic Reduction of Carbon Dioxide: Opportunities with Heterogeneous Molecular Catalysts. *Energy Environ. Sci.* **2020**, *13*, 374–403.

(16) Francke, R.; Schille, B.; Roemelt, M. Homogeneously Catalyzed Electroreduction of Carbon Dioxide—Methods, Mechanisms, and Catalysts. *Chem. Rev.* **2018**, *118*, 4631–4701.

(17) Fukuzumi, S.; Lee, Y.-M.; Ahn, H. S.; Nam, W. Mechanisms of Catalytic Reduction of CO_2 with Heme and Nonheme Metal Complexes. *Chem. Sci.* **2018**, *9*, 6017–6034.

(18) Hammouche, M.; Lexa, D.; Savéant, J. M.; Momenteau, M. Catalysis of the Electrochemical Reduction of Carbon Dioxide by Iron("0") Porphyrins. *J. Electroanal. Chem. Interfacial Electrochem.* **1988**, *249*, 347–351.

(19) Costentin, C.; Drouet, S.; Robert, M.; Savéant, J.-M. A Local Proton Source Enhances CO_2 Electroreduction to CO by a Molecular Fe Catalyst. *Science* **2012**, *338*, 90–94.

(20) Costentin, C.; Robert, M.; Savéant, J.-M.; Tatin, A. Efficient and Selective Molecular Catalyst for the CO_2-to-CO Electrochemical Conversion in Water. *Proc. Natl. Acad. Sci.* **2015**, *112*, 6882–6886.

(21) Costentin, C.; Passard, G.; Robert, M.; Savéant, J.-M. Ultraefficient Homogeneous Catalyst for the CO_2-to-CO Electrochemical Conversion. *Proc. Natl. Acad. Sci.* **2014**, *111*, 14990–14994.

(22) Azcarate, I.; Costentin, C.; Robert, M.; Savéant, J.-M. Through-Space Charge Interaction Substituent Effects in Molecular Catalysis Leading to the Design of the Most Efficient Catalyst of CO_2-to-CO Electrochemical Conversion. *J. Am. Chem. Soc.* **2016**, *138*, 16639–16644.

(23) Rao, H.; Lim, C.-H.; Bonin, J.; Miyake, G. M.; Robert, M. Visible-Light-Driven Conversion of CO_2 to CH_4 with an Organic Sensitizer and an Iron Porphyrin Catalyst. *J. Am. Chem. Soc.* **2018**, *140*, 17830–17834.

(24) Rao, H.; Schmidt, L. C.; Bonin, J.; Robert, M. Visible-Light-Driven Methane Formation from CO_2 with a Molecular Iron Catalyst. *Nature* **2017**, *548*, 74–77.

(25) Martin, D. J.; Mayer, J. M. Oriented Electrostatic Effects on O_2 and CO_2 Reduction by a Polycationic Iron Porphyrin. *J. Am. Chem. Soc.* **2021**, *143*, 11423–11434.

(26) Masaoka, S.; Kosugi, K.; Kondo, M. Quick and Easy Method for Dramatic Improvement of the Electrochemical CO_2 Reduction Activity of an Iron Porphyrin Complex. *Angew. Chem. Int. Ed.*, **2021**, *60*, 22070–22074.

(27) Costentin, C.; Savéant, J.-M. Towards an Intelligent Design of Molecular Electrocatalysts. *Nat. Rev. Chem.* **2017**, *1*, 0087.

(28) Costentin, C.; Robert, M.; Savéant, J.-M. Current Issues in Molecular Catalysis Illustrated by Iron Porphyrins as Catalysts of the CO_2-to-CO Electrochemical Conversion. *Acc. Chem. Res.* **2015**, *48*, 2996–3006.

(29) Khadhraoui, A.; Gotico, P.; Boitrel, B.; Leibl, W.; Halime, Z.; Aukauloo, A. Local Ionic Liquid Environment at a Modified Iron Porphyrin Catalyst Enhances the Electrocatalytic Performance of

CO_2 to CO Reduction in Water. *Chem. Commun.* **2018**, *54*, 11630–11633.

(30) Zee, D. Z.; Nippe, M.; King, A. E.; Chang, C. J.; Long, J. R. Tuning Second Coordination Sphere Interactions in Polypyridyl–Iron Complexes to Achieve Selective Electrocatalytic Reduction of Carbon Dioxide to Carbon Monoxide. *Inorg. Chem.* **2020**, *59*, 5206–5217.

(31) Loipersberger, M.; Zee, D. Z.; Panetier, J. A.; Chang, C. J.; Long, J. R.; Head-Gordon, M. Computational Study of an Iron(II) Polypyridine Electrocatalyst for CO_2 Reduction: Key Roles for Intramolecular Interactions in CO_2 Binding and Proton Transfer. *Inorg. Chem.* **2020**, *59*, 8146–8160.

(32) Che, C.-M.; Chan, C.-W.; Yang, S.-M.; Guo, C.-X.; Lee, C.-Y.; Peng, S.-M. Synthesis, Properties and Crystal Structures of Iron-(II) and -(III) Complexes of 2,2′:6′,2″:6″,2‴-Quaterpyridine. *J. Chem. Soc. Dalton Trans.* **1995**, *18*, 2961–2966.

(33) Cometto, C.; Chen, L.; Lo, P.-K.; Guo, Z.; Lau, K.-C.; Anxolabéhère-Mallart, E.; Fave, C.; Lau, T.-C.; Robert, M. Highly Selective Molecular Catalysts for the CO_2-to-CO Electrochemical Conversion at Very Low Overpotential. Contrasting Fe vs Co Quaterpyridine Complexes upon Mechanistic Studies. *ACS Catal.* **2018**, *8*, 3411–3417.

(34) Cometto, C.; Chen, L.; Anxolabéhère-Mallart, E.; Fave, C.; Lau, T.-C.; Robert, M. Molecular Electrochemical Catalysis of the CO_2-to-CO Conversion with a Co Complex: A Cyclic Voltammetry Mechanistic Investigation. *Organometallics* **2019**, *38*, 1280–1285.

(35) Loipersberger, M.; Cabral, D. G. A.; Chu, D. B. K.; Head-Gordon, M. Mechanistic Insights into Co and Fe Quaterpyridine-Based CO_2 Reduction Catalysts: Metal–Ligand Orbital Interaction as the Key Driving Force for Distinct Pathways. *J. Am. Chem. Soc.* **2021**, *143*, 744–763.

(36) Smith, P. T.; Nichols, E. M.; Cao, Z.; Chang, C. J. Hybrid Catalysts for Artificial Photosynthesis: Merging Approaches from Molecular, Materials, and Biological Catalysis. *Acc. Chem. Res.* **2020**, *53*, 575–587.

(37) Zee, D. Z.; Chantarojsiri, T.; Long, J. R.; Chang, C. J. Metal–Polypyridyl Catalysts for Electro- and Photochemical Reduction of Water to Hydrogen. *Acc. Chem. Res.* **2015**, *48*, 2027–2036.

(38) Smith, P. T.; Weng, S.; Chang, C. J. An NADH-Inspired Redox Mediator Strategy to Promote Second-Sphere Electron and Proton Transfer for Cooperative Electrochemical CO_2 Reduction Catalyzed by Iron Porphyrin. *Inorg. Chem.* **2020**, *59*, 9270–9278.

(39) Derrick, J. S.; Loipersberger, M.; Chatterjee, R.; Iovan, D. A.; Smith, P. T.; Chakarawet, K.; Yano, J.; Long, J. R.; Head-Gordon, M.; Chang, C. J. Metal–Ligand Cooperativity via Exchange Coupling Promotes Iron- Catalyzed Electrochemical CO_2 Reduction at Low Overpotentials. *J. Am. Chem. Soc.* **2020**, *142*, 20489–20501.

(40) Matsubara, Y. Unified Benchmarking of Electrocatalysts in Noninnocent Second Coordination Spheres for CO_2 Reduction. *ACS Energy Lett.* **2019**, *4*, 1999–2004.

(41) Coetzee, J. F.; Padmanabhan, G. R. Dissociation and Homoconjugation of Certain Phenols in Acetonitrile. *J. Phys. Chem.* **1965**, *69*, 3193–3196.

(42) Fourmond, V.; Jacques, P.-A.; Fontecave, M.; Artero, V. H_2 Evolution and Molecular Electrocatalysts: Determination of Overpotentials and Effect of Homoconjugation. *Inorg. Chem.* **2010**, *49*, 10338–10347.

(43) Stratakes, B. M.; Dempsey, J. L.; Miller, A. J. M. Determining the Overpotential of Electrochemical Fuel Synthesis Mediated by Molecular Catalysts: Recommended Practices, Standard Reduction Potentials, and Challenges. *ChemElectroChem* **2021**, *8*, 4161–4180.

(44) Rountree, E. S.; McCarthy, B. D.; Eisenhart, T. T.; Dempsey, J. L. Evaluation of Homogeneous Electrocatalysts by Cyclic Voltammetry. *Inorg. Chem.* **2014**, *53*, 9983–10002.

(45) Lee, K. J.; Elgrishi, N.; Kandemir, B.; Dempsey, J. L. Electrochemical and Spectroscopic Methods for Evaluating Molecular Electrocatalysts. *Nat. Rev. Chem.* **2017**, *1*, 0039.

(46) Costentin, C.; Savéant, J.-M. Multielectron, Multistep Molecular Catalysis of Electrochemical Reactions: Benchmarking of Homogeneous Catalysts. *ChemElectroChem* **2014**, *1*, 1226–1236.

(47) Wang, V. C.-C.; Johnson, B. A. Interpreting the Electrocatalytic Voltammetry of Homogeneous Catalysts by the Foot of the Wave Analysis and Its Wider Implications. *ACS Catal.* **2019**, *9*, 7109–7123.

(48) Costentin, C.; Passard, G.; Savéant, J.-M. Benchmarking of Homogeneous Electrocatalysts: Overpotential, Turnover Frequency, Limiting Turnover Number. *J. Am. Chem. Soc.* **2015**, *137*, 5461–5467.

(49) Costentin, C.; Drouet, S.; Robert, M.; Savéant, J.-M. Turnover Numbers, Turnover Frequencies, and Overpotential in Molecular Catalysis of Electrochemical Reactions. Cyclic Voltammetry and Preparative-Scale Electrolysis. *J. Am. Chem. Soc.* **2012**, *134*, 11235–

(50) Costentin, C.; Drouet, S.; Robert, M.; Savéant, J.-M. Correction to Turnover Numbers, Turnover Frequencies, and Overpotential in Molecular Catalysis of Electrochemical Reactions. Cyclic Voltammetry and Preparative-Scale Electrolysis. *J. Am. Chem. Soc.* **2012**, *134*, 19949–19950.

(51) Thom, A. J. W.; Sundstrom, E. J.; Head-Gordon, M. LOBA: A Localized Orbital Bonding Analysis to Calculate Oxidation States, with Application to a Model Water Oxidation Catalyst. *Phys. Chem. Chem. Phys.* **2009**, *11*, 11297–11304.

(52) Epifanovsky, E.; Gilbert, A. T. B.; Feng, X.; Lee, J.; Mao, Y.; Mardirossian, N.; Pokhilko, P.; White, A. F.; Coons, M. P.; Dempwolff, A. L.; Gan, Z.; Hait, D.; Horn, P. R.; Jacobson, L. D.; Kaliman, I.; Kussmann, J.; Lange, A. W.; Lao, K. U.; Levine, D. S.; Liu, J.; McKenzie, S. C.; Morrison, A. F.; Nanda, K. D.; Plasser, F.; Rehn, D. R.; Vidal, M. L.; You, Z.-Q.; Zhu, Y.; Alam, B.; Albrecht, B. J.; Aldossary, A.; Alguire, E.; Andersen, J. H.; Athavale, V.; Barton, D.; Begam, K.; Behn, A.; Bellonzi, N.; Bernard, Y. A.; Berquist, E. J.; Burton, H. G. A.; Carreras, A.; Carter-Fenk, K.; Chakraborty, R.; Chien, A. D.; Closser, K. D.; Cofer-Shabica, V.; Dasgupta, S.; de Wergifosse, M.; Deng, J.; Diedenhofen, M.; Do, H.; Ehlert, S.; Fang, P.-T.; Fatehi, S.; Feng, Q.; Friedhoff, T.; Gayvert, J.; Ge, Q.; Gidofalvi, G.; Goldey, M.; Gomes, J.; González-Espinoza, C. E.; Gulania, S.; Gunina, A. O.; Hanson-Heine, M. W. D.; Harbach, P. H. P.; Hauser, A.; Herbst, M. F.; Hernández Vera, M.; Hodecker, M.; Holden, Z. C.; Houck, S.; Huang, X.; Hui, K.; Huynh, B. C.; Ivanov, M.; Jász, Á.; Ji, H.; Jiang, H.; Kaduk, B.; Kähler, S.; Khistyaev, K.; Kim, J.; Kis, G.; Klunzinger, P.; Koczor-Benda, Z.; Koh, J. H.; Kosenkov, D.; Koulias, L.; Kowalczyk, T.; Krauter, C. M.; Kue, K.; Kunitsa, A.; Kus, T.; Ladjánszki, I.; Landau, A.; Lawler, K. V.; Lefrancois, D.; Lehtola, S.; Li, R. R.; Li, Y.-P.; Liang, J.; Liebenthal, M.; Lin, H.-H.; Lin, Y.-S.; Liu, F.; Liu, K.-Y.; Loipersberger, M.; Luenser, A.; Manjanath, A.; Manohar, P.; Mansoor, E.; Manzer, S. F.; Mao, S.-P.; Marenich, A. V.; Markovich, T.; Mason, S.; Maurer, S. A.; McLaughlin, P. F.; Menger, M. F. S. J.; Mewes, J.-M.; Mewes, S. A.; Morgante, P.; Mullinax, J. W.; Oosterbaan, K. J.; Paran, G.; Paul, A. C.; Paul, S. K.; Pavošević, F.; Pei, Z.; Prager, S.; Proynov, E. I.; Rák, Á.; Ramos-Cordoba, E.; Rana, B.; Rask, A. E.; Rettig, A.; Richard, R. M.; Rob, F.; Rossomme, E.; Scheele, T.; Scheurer, M.; Schneider, M.; Sergueev, N.; Sharada, S. M.; Skomorowski, W.; Small, D. W.; Stein, C. J.; Su, Y.-C.; Sundstrom, E. J.; Tao, Z.; Thirman, J.; Tornai, G. J.; Tsuchimochi, T.; Tubman, N. M.; Veccham, S. P.; Vydrov, O.; Wenzel, J.; Witte, J.; Yamada, A.; Yao, K.; Yeganeh, S.; Yost, S. R.; Zech, A.; Zhang, I. Y.; Zhang, X.; Zhang, Y.; Zuev, D.; Aspuru-Guzik, A.; Bell, A. T.; Besley, N. A.; Bravaya, K. B.; Brooks, B. R.; Casanova, D.; Chai, J.-D.; Coriani, S.; Cramer, C. J.; Cserey, G.; DePrince, A. E.; DiStasio, R. A.; Dreuw, A.; Dunietz, B. D.; Furlani, T. R.; Goddard, W. A.; Hammes-Schiffer, S.; Head-Gordon, T.; Hehre, W. J.; Hsu, C.-P.; Jagau, T.-C.; Jung, Y.; Klamt, A.; Kong, J.; Lambrecht, D. S.; Liang, W.; Mayhall, N. J.; McCurdy, C. W.; Neaton, J. B.; Ochsenfeld, C.; Parkhill, J. A.; Peverati, R.; Rassolov, V. A.; Shao, Y.; Slipchenko, L. V.; Stauch, T.; Steele, R. P.; Subotnik, J. E.; Thom, A. J. W.; Tkatchenko, A.; Truhlar, D. G.; Van Voorhis, T.; Wesolowski, T. A.; Whaley, K. B.; Woodcock, H. L.; Zimmerman, P. M.; Faraji, S.; Gill, P. M. W.; Head-Gordon, M.; Herbert, J. M.; Krylov, A. I. Software for the Frontiers of Quantum Chemistry:

An Overview of Developments in the Q-Chem 5 Package. *J. Chem. Phys.* **2021**, *155*, 084801.

(53) Kelly, C. P.; Cramer, C. J.; Truhlar, D. G. Single-Ion Solvation Free Energies and the Normal Hydrogen Electrode Potential in Methanol, Acetonitrile, and Dimethyl Sulfoxide. *J. Phys. Chem. B* **2007**, *111*, 408–422.

(54) Konezny, S. J.; Doherty, M. D.; Luca, O. R.; Crabtree, R. H.; Soloveichik, G. L.; Batista, V. S. Reduction of Systematic Uncertainty in DFT Redox Potentials of Transition-Metal Complexes. *J. Phys. Chem. C* **2012**, *116*, 6349–6356.

(55) Song, J.; Klein, E. L.; Neese, F.; Ye, S. The Mechanism of Homogeneous CO_2 Reduction by Ni(Cyclam): Product Selectivity, Concerted Proton–Electron Transfer and C–O Bond Cleavage. *Inorg. Chem.* **2014**, *53*, 7500–7507.

(56) Fu, Y.; Liu, L.; Yu, H.-Z.; Wang, Y.-M.; Guo, Q.-X. Quantum-Chemical Predictions of Absolute Standard Redox Potentials of Diverse Organic Molecules and Free Radicals in Acetonitrile. *J. Am. Chem. Soc.* **2005**, *127*, 7227–7234.

(57) Weigend, F.; Ahlrichs, R. Balanced Basis Sets of Split Valence, Triple Zeta Valence and Quadruple Zeta Valence Quality for H to Rn: Design and Assessment of Accuracy. *Phys. Chem. Chem. Phys.* **2005**, *7*, 3297–3305.

(58) Karton, A.; O'Reilly, R. J.; Radom, L. Assessment of Theoretical Procedures for Calculating Barrier Heights for a Diverse Set of Water-Catalyzed Proton-Transfer Reactions. *J. Phys. Chem. A* **2012**, *116*, 4211–4221.

(59) Mardirossian, N.; Head-Gordon, M. Thirty Years of Density Functional Theory in Computational Chemistry: An Overview and Extensive Assessment of 200 Density Functionals. *Mol. Phys.* **2017**, *115*, 2315–2372.

(60) Bhattacharjee, A.; Andreiadis, E. S.; Chavarot-Kerlidou, M.; Fontecave, M.; Field, M. J.; Artero, V. A Computational Study of the Mechanism of Hydrogen Evolution by Cobalt(Diimine-Dioxime) Catalysts. *Chem. – Eur. J.* **2013**, *19*, 15166–15174.

(61) Raamat, E.; Kaupmees, K.; Ovsjannikov, G.; Trummal, A.; Kütt, A.; Saame, J.; Koppel, I.; Kaljurand, I.; Lipping, L.; Rodima, T.; Pihl, V.; Koppel, I. A.; Leito, I. Acidities of Strong Neutral Brønsted Acids in Different Media. *J. Phys. Org. Chem.* **2013**, *26*, 162–170.

(62) Kozuch, S.; Shaik, S. How to Conceptualize Catalytic Cycles? The Energetic Span Model. *Acc. Chem. Res.* **2011**, *44*, 101–110.

(63) Gonell, S.; Lloret-Fillol, J.; Miller, A. J. M. An Iron Pyridyl-Carbene Electrocatalyst for Low Overpotential CO_2 Reduction to CO. *ACS Catal.* **2021**, *11*, 615–626.

(64) Kozuch, S.; Shaik, S. A Combined Kinetic–Quantum Mechanical Model for Assessment of Catalytic Cycles: Application to Cross-Coupling and Heck Reactions. *J. Am. Chem. Soc.* **2006**, *128*, 3355–3365.

(65) Uhe, A.; Kozuch, S.; Shaik, S. Automatic Analysis of Computed Catalytic Cycles. *J. Comput. Chem.* **2011**, *32*, 978–985.

(66) Kozuch, S. A Refinement of Everyday Thinking: The Energetic Span Model for Kinetic Assessment of Catalytic Cycles. *WIREs Comput. Mol. Sci.* **2012**, *2*, 795–815.

(67) Mao, Y.; Loipersberger, M.; Kron, K. J.; Derrick, J. S.; Chang, C. J.; Sharada, S. M.; Head-Gordon, M. Consistent Inclusion of Continuum Solvation in Energy Decomposition Analysis: Theory and Application to Molecular CO_2 Reduction Catalysts. *Chem. Sci.* **2021**, *12*, 1398–1414.

(68) Mao, Y.; Loipersberger, M.; Horn, P. R.; Das, A.; Demerdash, O.; Levine, D. S.; Prasad Veccham, S.; Head-Gordon, T.; Head-Gordon, M. From Intermolecular Interaction Energies and Observable Shifts to Component Contributions and Back Again: A Tale of Variational Energy Decomposition Analysis. *Annu. Rev. Phys. Chem.* **2021**, *72*, 641–666.

(69) Ambre, R. B.; Daniel, Q.; Fan, T.; Chen, H.; Zhang, B.; Wang, L.; Ahlquist, M. S. G.; Duan, L.; Sun, L. Molecular Engineering for Efficient and Selective Iron Porphyrin Catalysts for Electrochemical Reduction of CO_2 to CO. *Chem. Commun.* **2016**, *52*, 14478–14481.

(70) Khaliullin, R. Z.; Cobar, E. A.; Lochan, R. C.; Bell, A. T.; Head-Gordon, M. Unravelling the Origin of Intermolecular Interactions Using Absolutely Localized Molecular Orbitals. *J. Phys. Chem. A* **2007**, *111*, 8753–8765.

SYNOPSIS TOC: $[Fe(tpyPY2Me)]^{2+}$ ($[Fe]^{2+}$) is a homogeneous electrocatalyst for converting CO_2 into CO at low overpotentials with high selectivity and fast rates. Here we report a combined computational and experimental study that establishes two distinct mechanistic pathways for electrochemical CO_2 reduction catalyzed by $[Fe]^{2+}$ as a function of applied potential. Determination of mechanistic pathways is then used to direct the computational exploration of improved ligand framework design by energy decomposition analysis.